This is a pre-copyedited, author-produced PDF of an article accepted for publication in Geophysical Journal International following peer review. The version of record "Satoru Baba, Shunsuke Takemura, Kazushige Obara, Akiko Takeo, Yusuke Yamashita, Masanao Shinohara, Spatial variation in shallow slow earthquake activity in Hyuga-nada, southwest Japan" is available online at https://doi.org/10.1093/gji/ggae039.

Spatial variation in shallow slow earthquake activity in Hyuga-nada, southwest Japan

Satoru Baba[1,2], Shunsuke Takemura[1], Kazushige Obara[1], Akiko Takeo[1], Yusuke Yamashita[3], and Masanao Shinohara[1]

1. Earthquake Research Institute, the University of Tokyo, 1-1-1, Yayoi, Bunkyo-ku, Tokyo, 113-0032, Japan
2. Now at Japan Agency for Marine-Earth Science and Technology, 2-15, Natsushima-cho, Yokosuka, Kanagawa, 237-0061, Japan
3. Miyazaki Observatory, Disaster Prevention Research Institute, Kyoto University, 3884 Kaeda, Miyazaki, Miyazaki, 889-2161, Japan

Abbreviated title: Spatial variation in slow earthquakes in Hyuga-nada

Corresponding author: Satoru Baba
E-mail: babasatoru@jamstec.go.jp
Phone: +81-46-867-9342

Summary

Hyuga-nada, off the Pacific coast of Kyushu along the Nankai Trough in southwest Japan, is one of the most active slow earthquake regions around Japan. We estimated the energies of shallow tremors and moments of shallow very low frequency earthquakes (VLFEs) in Hyuga-nada using data from a permanent onshore broadband network and temporary ocean bottom seismometer observations. The energies and moments of these slow earthquakes have a similar along-strike variation and are generally higher south of the subducted Kyushu-Palau Ridge than near the top of the ridge. This spatial variation is also related to the characteristics of slow earthquake migration. The along-strike migration speed was faster at initiation in the south, where the moments of slow earthquakes are higher. After migration entered the subducted Kyushu-Palau Ridge, its speed was decelerated with a parabolic pattern and their moments became smaller. Assuming a constant patch size of slow earthquakes, we estimated that the stress drop of VLFEs in the south of the subducted ridge was approximately three times higher than that near the top of the subducted ridge. According to our observations and a physical model, this stress drop difference between adjacent regions may cause parabolic migration. We also estimated the scaled energy of slow earthquakes from the ratio of the seismic energy rates of tremors to the seismic moment rates of accompanying VLFEs. The spatial variation in scaled energy is not identified inside the Hyuga-nada. Since the range of scaled energy is similar between the south and near the top of the subducted ridge, the apparent stress may be similar if the rigidity is the same. The dominant range of scaled energy of slow earthquakes in Hyuga-nada is $10^{-11.5}$–$10^{-8.5}$. In addition to having similar or one order smaller values compared to other slow earthquake regions, the range of scaled energy in Hyuga-nada is broader. This broader range suggests wide range of characteristic time and various spectral features of slow earthquakes in Hyuga-nada. Based on a Brownian slow earthquake model, the wide range of characteristic time in this area suggests width variations of slow earthquake source area.

Keywords: Subduction zone processes, Seismicity and tectonics, Earthquake source observations, Japan

1. Introduction

After the discovery of tectonic low frequency tremors by Obara (2002), slow earthquakes, which are fault slips with longer characteristic durations than regular earthquakes with the same seismic moment (e.g., Ide et al. 2007a; 2008; Ide & Beroza 2023; Wang et al. 2023), were mainly detected around seismogenic zones on plate boundaries of subduction zones or strike slip regimes in the world. Seismic slow earthquakes are classified into tremors and low frequency earthquakes observed in a frequency range of 2–8 Hz (e.g., Shelly et al. 2006) and very low frequency earthquakes (VLFEs) observed in a frequency range of 0.02–0.05 Hz (e.g., Obara & Ito 2005). Slow slip events (SSEs) are geodetically observed as crustal deformations, with duration ranging from several days to several years (e.g., Dragert et al. 2001; Hirose et al. 1999). The focal mechanisms of slow earthquakes in subduction zones are thrust-type and consistent with those of megathrust earthquakes along plate boundaries (e.g., Ide et al. 2007b; Ito et al. 2007; Takemura et al. 2019). In addition, slow earthquake activity can reflect the stress conditions on the plate boundary around the slow earthquake regions (e.g., Obara & Kato 2016). Recent studies have revealed that slow earthquakes can potentially trigger megathrust earthquakes. An SSE occurred before the 2011 Tohoku earthquake in Japan (e.g., Kato et al. 2012), the 2012 Nicoya Peninsula earthquake in Costa Rica (e.g., Voss et al. 2018), and the 2014 Iquique earthquake in Chile (e.g., Ruiz et al., 2014). Thus, studies of slow earthquakes are important for understanding the slip behaviours on the plate boundary and the occurrence mechanism of megathrust earthquakes.

Around the Japanese islands, slow earthquakes occur in shallower and deeper extensions of the seismogenic zone in southwest Japan along the Nankai Trough and in the offshore region of northeastern Japan along the Japan Trench. In Hyuga-nada, off the Pacific coast of Kyushu, VLFEs are the most active around Japan (Baba *et al.* 2020). In this area, Asano et al. (2015) reported the migration of shallow VLFEs, which can be considered as a proxy for rupture propagation of an SSE (e.g., Bartlow et al. 2011; Ito et al. 2007), in 2010 (Fig. 1a). VLFEs first migrated from 30.5º N to 31.5º N along the strike direction and changed to along-dip migration at the subducted Kyushu-Palau Ridge, which is subducting at the Nankai Trough. Although VLFEs are observed by onshore stations owing to the effective propagation of surface waves along shallower low velocity structures, it is difficult to identify weak signals of shallow tremors in Hyuga-nada using permanent onshore stations. Yamashita et al. (2015) and Yamashita et al. (2021) detected shallow tremors and reported their migrations in Hyuga-nada utilizing temporary ocean bottom seismometers (OBSs) in 2013 and 2015, respectively (Fig. 1b and c). In 2013, tremors migrated twice from 30.3º N to 31.7º N. In 2015, tremors migrated from west to east, north of 31º N and extended near the trench axis (Yamashita et al. 2021). The shallow tremors in Hyuga-nada were temporally correlated with shallow VLFEs (Fig. 2). The spatial distributions of

tremors in both 2013 and 2015 were contained by those of VLFEs in 2010. Temporary OBS observations also revealed a high-resolution distribution of VLFEs. Tonegawa et al. (2020) suggested that the depths of shallow VLFEs near the subducted Kyushu-Palau Ridge are approximately 5 km different from the surrounding area.

The tectonic regime in Hyuga-nada is very characteristic; the Kyushu-Palau Ridge is subducting and the trench axis bends around the region where the ridge subducts (Fig. 1). In addition, repeating earthquakes representing quasi-static slips on the plate boundary (e.g., Nadeau & McEvilly 1999; Uchida et al. 2003) occur in the downdip of shallow slow earthquakes (e.g., Igarashi, 2020; Yamashita et al., 2012). Tectonic conditions, such as a subducted ridge or horizontal heterogeneity of pore fluid pressure around the plate boundary, can affect the source parameters, such as the moment rate, of slow earthquakes (Baba et al. 2020; Takemura et al. 2022b). To investigate the spatial relationships between slow earthquake activity and tectonic conditions in Hyuga-nada, we quantitatively estimated the spatial variation in the source characteristics of slow earthquakes at high spatial resolution using onshore and offshore data.

As the quantitative indicators of source characteristics, we focus on the energy rate functions of tremors, moment rate functions of VLFEs, and the scaled energy. Recently, slow earthquake signals have been also detected in the microseism frequency band between tremors and VLFEs (Kaneko et al. 2018; Masuda et al. 2020; Yamashita et al. 2021); therefore, slow earthquakes are assumed to be broadband phenomena (Ide & Maury, 2018). Ide et al. (2008) demonstrated the seismic energy rates of slow earthquakes in 2–8 Hz are proportional to the seismic moment rates and evaluated the scaled energy of slow earthquakes by the ratio between tremor energy rate and the accompanying VLFE moment rate. Scaled energy has been used for the purpose of comparing dynamic characteristics of seismic events (Kanamori & Rivera 2006). If the rupture process of seismic events is self-similar, the scaled energy is constant. Previous studies demonstrated that scaled energy of slow earthquakes is 10^{-10}–10^{-8} and 4–5 orders smaller than that of regular earthquakes (e.g., Ide et al. 2008). Yabe et al. (2019) and Yabe et al. (2021) estimated the scaled energy of shallow slow earthquakes along the Nankai Trough and along the Japan Trench, respectively, and suggested the relationship between scaled energy distribution and geological condition. To investigate the characteristics of broadband slow earthquakes as well as the spatial relationships between slow earthquake activity and tectonic conditions, we evaluated the energy rate functions of tremors, the moment rate functions of VLFEs, and the scaled energy of the slow earthquakes in Hyuga-nada at a high spatial resolution using onshore and offshore data.

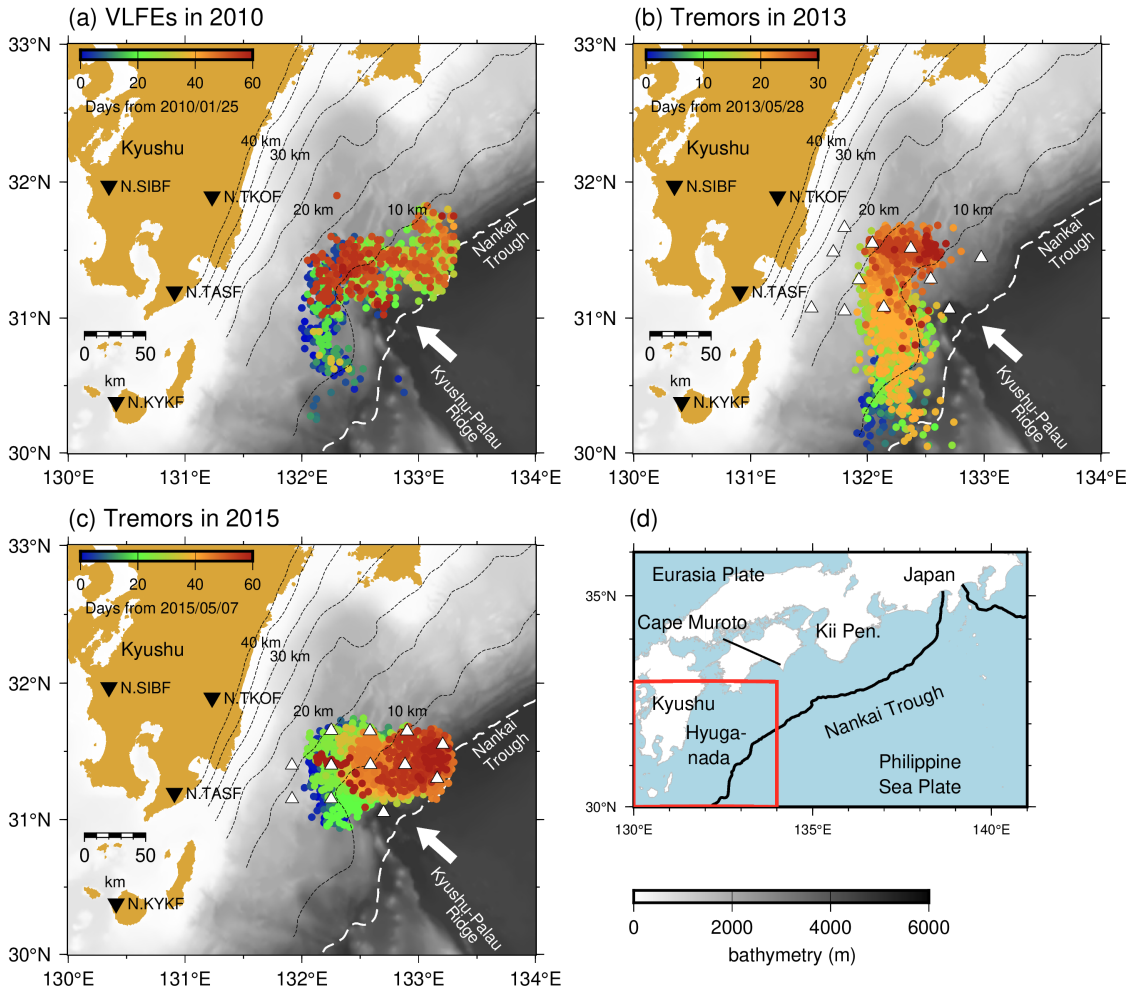

Figure 1. Slow earthquake activity in Hyuga-nada. Coloured dots are epicentres of (a) shallow VLFEs in 2010 detected by Asano et al. (2015), (b) shallow tremors in 2013 detected by Yamashita et al. (2015), and (c) shallow tremors in 2015 detected by Yamashita et al. (2021). The colours of dots correspond to days from the first activity for each tremor episode. Blue and red dots indicate epicentres of tremors that occurred at the beginning and end of the migration episode, respectively. White triangles represent the locations of the OBSs utilized in the shallow tremor analysis. Inverted triangles exhibit the locations of the F-net stations utilized in the shallow VLFE analysis. White arrows indicate the direction of the motion of the Philippine Sea Plate relative to the Eurasia Plate (NUVEL-1A; DeMets et al., 1994). White dashed lines represent the trench axis. Background grey scale denotes the bathymetry (ETOPO1; Amante & Eakins 2009). Dashed contours indicate the isodepth at the top of the Philippine Sea plate in intervals of 5 km (Nakanishi *et al.* 2018). (d) Tectonics of Hyuga-nada. The area surrounded by the red rectangle is shown in Figs. 1a-c. Black lines represent the boundaries between the plates.

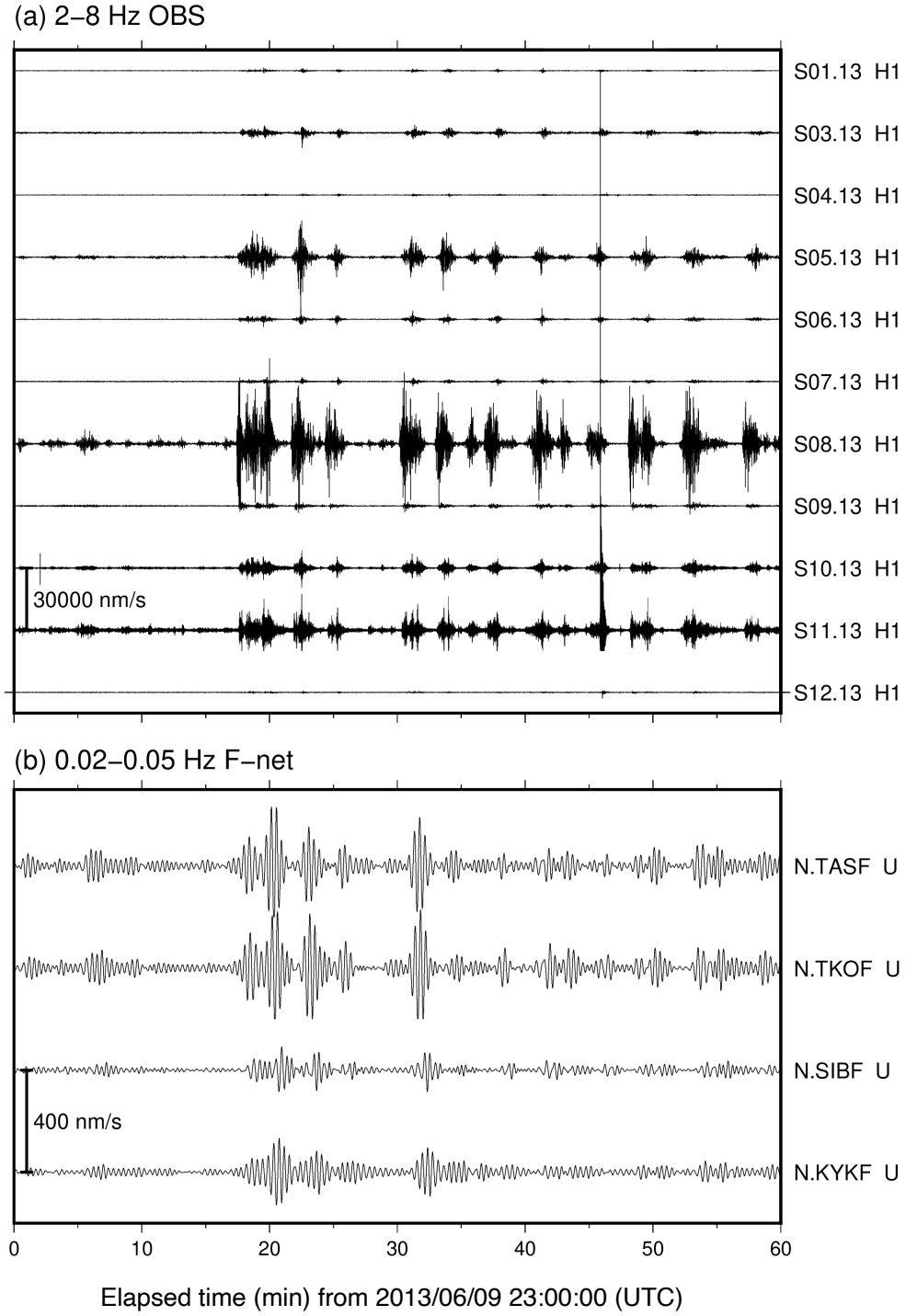

Figure 2. Example of one-hour records for (a) shallow tremors in a frequency range of 2–8 Hz at OBSs and (b) shallow VLFEs in a frequency range of 0.02–0.05 Hz at F-net stations.

2. Data and Method

2.1. Estimation of energy rate functions of tremors

For the analysis of tremors, we evaluated the energy rate functions of tremors located by Yamashita et al. (2015; 2021). We used 360 s broadband (NK1508 and NK1510 in 2015), 1 Hz (S06.13, S09.13 in 2013 and others in 2015) and 4.5 Hz (others in 2013) short-period OBS records of temporary seismological observations in Hyuga-nada. 11 and 12 OBSs were installed for observations from April 17 to July 4, 2013 (Yamashita et al. 2015) and from January 1, 2015 to January 1, 2016 (Yamashita et al. 2021), respectively. The sampling rates were 200 Hz (S05.13, S06.13, S08.13, and S09.13 in 2013 and all OBSs in 2015) or 128 Hz (other OBSs in 2013). Analog seismic signals were digitized using a 16-, 20-, or 24-bit A/D converter. After instrumental responses were removed, a bandpass filter was applied in a frequency range of 2–8 Hz. Then, the vertical and horizontal components of the root-mean-square (RMS) velocity envelopes were calculated with a smoothing time window of 5 s. The envelopes were resampled at one sample per second. Examples of envelope waveforms of a tremor obtained by the RMS of the sums squared seismograms of two horizontal components are displayed in Fig. 3. Since OBSs are often installed on soft sediments, amplitudes of seismic waves are more amplified compared to onshore stations. We therefore selected a permanent onshore station N.TASF from the F-net broadband seismograph network (Aoi *et al.* 2020) as a reference station, because F-net stations are installed at inland outcrop rock sites (Aoi et al., 2020) and the site amplification factors between F-net stations are very similar (Takemoto *et al.* 2012).

We estimated the site amplification factors of the vertical and horizontal components at each OBS relative to N.TASF at 2–8 Hz and the quality factor of the *S*-wave attenuation (Q) by utilizing the information of the maximum *S*-wave amplitudes of intraslab regular earthquakes following the method of Yabe et al. (2019). The maximum *S*-wave amplitude of the i-th earthquake at the j-th station (A_{ij}) is expressed by the following relationship:

$$\ln(A_{ij}) = \ln(S_i) - \ln(\sqrt{4\pi}L_{ij}) - \frac{\pi f_c Q^{-1}}{V_S} L_{ij} + \ln(C_j) \quad (1)$$

where S_i is the size of the i-th seismic source, L_{ij} is the distance between the hypocentre of the i-th earthquake and the j-th station, f_c represents the central frequency (5 Hz in this study), V_s is the *S*-wave velocity (assuming 3.5 km/s; after Yabe et al, 2019; 2021), and C_j is the site amplification factor. Q^{-1} represents apparent S-wave attenuation, including intrinsic and scattering attenuations. The attenuation by geometrical spreading corresponds to the second term of the right-hand side of the equation (1). We measured the maximum *S*-wave amplitudes of regular earthquakes more than 5 km deeper than the plate boundary of the Japan Integrated Velocity Structure Model (JIVSM; Koketsu et al. 2012) with magnitudes larger than 2.5 listed in the regular earthquake catalogue of the Japan Meteorological Agency (Fig. S1). We defined the maximum envelope

amplitude of the time window from 2 s before to 50 s after the arrival time at each OBS as the maximum *S*-wave amplitude. To estimate the site amplification factor of *j*-th station relative to a reference station (j_0), taking the difference of equation (1) for *i*-th event at *j*-th and the reference station:

$$ln\left(\frac{A_{ij}}{A_{ij_0}}\right) + ln\left(\frac{L_{ij}}{L_{ij_0}}\right) = -\frac{\pi f_c Q^{-1}}{V_S}(L_{ij} - L_{ij_0}) + ln\left(\frac{C_j}{C_{j_0}}\right). \quad (2)$$

The site amplification factor relative to N.TASF and Q^{-1} at each OBS was estimated by solving Equation (2) using the least-squares method. Following Yabe et al. (2019), we set the site amplification factor at the reference station N.TASF as 2 to consider the free-surface effect. In the following steps, we utilized the RMS of the sums of the squared three-component seismograms with a smoothing time window of 5 s after site correction by implementing the site amplification factors displayed in Fig. 4. After correcting the site amplification factors, the amplitudes were normalized by the site conditions at the reference onshore station, N.TASF. We also evaluated the average of Q^{-1} solved at each OBS in Equation (2) as $(3.4415\pm0.9585)\times10^{-3}$. We adopted this value to estimate the energy rate functions of the tremors.

We calculated the energy rate functions of the tremors by implementing the site amplification factors and Q^{-1} estimated by the above procedures. The energy rate function of a tremor ($E_j(t)$), estimated from the amplitudes of the *j*-th station, was calculated using the following equation:

$$E_j(t) = 2\pi V_S r_j^2 \rho A''^2_j\left(t + t_j\right)\exp\left(2\pi f_c Q^{-1} t_j\right) \quad (3)$$

where, $A''_j(t)$ is the amplitude of envelopes after the site-correction at the *j*-th station, r_j is the hypocentral distance from the tremor source to the *j*-th station, t_j is the travel time from the tremor source to the *j*-th station, and ρ is the density (assuming 2,700 kg/m^3 after Yabe et al, 2019; 2021). The epicentral locations of the tremors were set at those located by Yamashita et al. (2015; 2021). The depth of the tremors was set at the plate boundary of the JIVSM (Koketsu et al. 2012). To calculate the energy rate function, the time windows were set at 240 s, which started 60 s before the time window of the tremors set by Yamashita et al. (2015; 2021). We stacked the energy rate functions of a tremor for each station and estimated the average energy rate function $E_{\mathrm{ave}}(t)$ divided by the number of used stations. We calculated the cross-correlation coefficients (CCs) of the energy rate functions of all station pairs in Fig. 4 and further utilized the stations whose CCs exceeded 0.6 with at least one other station when stacking the energy rate functions.

The seismic energy *W* of a tremor is calculated by integrating $E_{\mathrm{ave}}(t)$ in the time range t_1–t_2:

$$W = \int_{t_1}^{t_2} E_{\mathrm{ave}}(t)dt. \quad (4)$$

The integration range is the period when the values of $E_{ave}(t)$ exceed 20% of the maximum

value of $E_{\mathrm{ave}}(t)$ (red line in the stacked energy rate function of Fig. 5). The duration of a tremor was defined as $t_2 - t_1$. The dominant range of tremor duration is 30–100 s. The seismic energy rate of the tremor was estimated by dividing the seismic energy by the duration. To evaluate the uncertainty of estimated energies, we calculated the standard deviation of the logarithm of energies estimated from each OBS data. The uncertainty of tremor energies is 0.5–1 order (Fig. S3a).

To validate the method of seismic energy estimation, we estimated seismic energies of regular earthquakes in the 2015–2016 observation by using the equations (3) and (4) (Fig. S4). The earthquakes in the area of 131.0ºE–133.5ºE and 30.0–32.0ºN with moment magnitudes larger than 4 by moment tensor analysis by F-net site (https://www.fnet.bosai.go.jp/event/search.php?LANG=en) were selected. In previous studies, scaled energies of regular earthquakes evaluated by the ratio of seismic energy to seismic moment are estimated to be approximately 3×10^{-5} (e.g., Ide & Beroza 2001). The scaled energies of most regular earthquakes shown in Fig. S4a are in the range of 10^{-5}–10^{-4} (Fig. S4b). It indicates that this method can estimate seismic energies on an order scale.

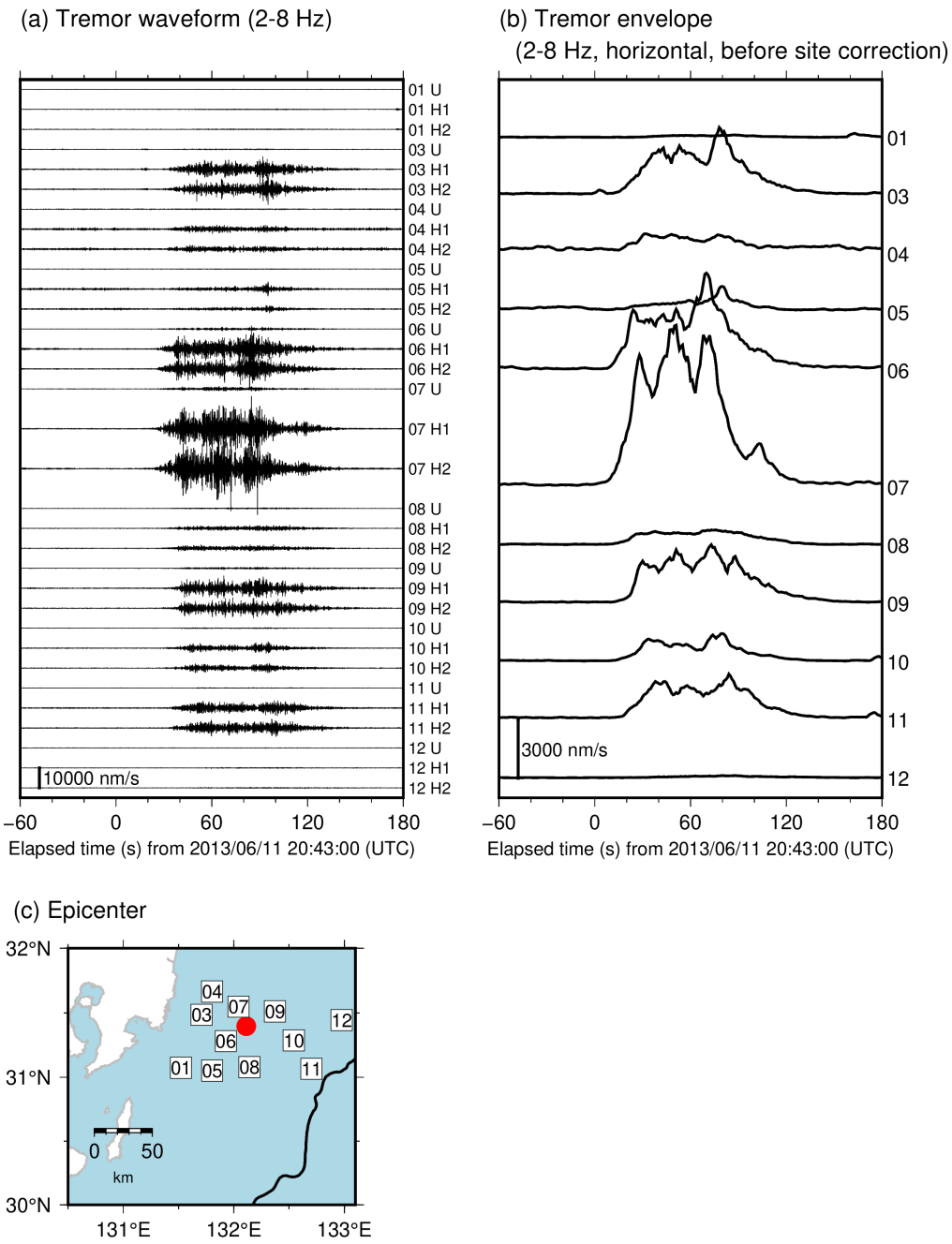

Figure 3. Example of (a) waveforms of a tremor in a frequency range of 2–8 Hz, and (b) envelopes obtained by the root-mean-square of sums squared seismograms of two horizontal components. Waveforms are displayed from 20:43:00 (UTC), June 11, 2013. (c) Red circle depicts the epicentre of the tremor displayed in in Fig. 3a and b. Black line represents the trench axis. Squares indicate the locations of OBSs.

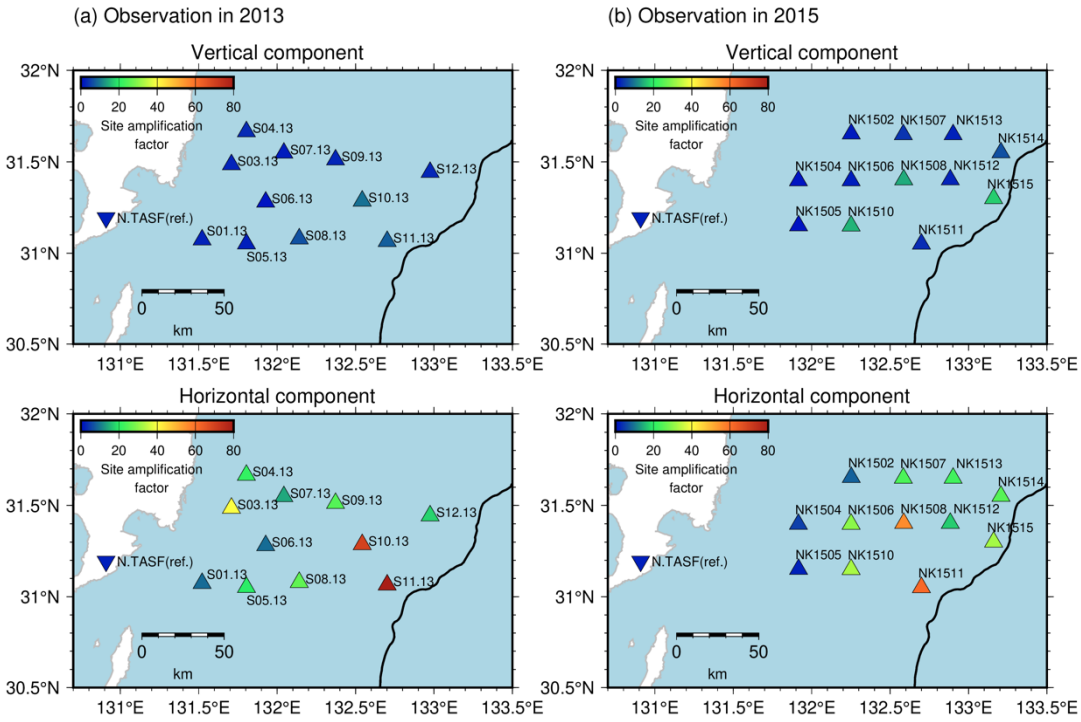

240

241 **Figure 4.** Site amplification factors at each OBS. Triangles represent the locations of OBSs.
242 Inverted triangle indicates the location of the reference station, N.TASF. Black line is the same as
243 displayed in Fig. 3. Estimation error of site amplification factors is shown in Fig. S2. Site
244 amplification factor at N.TASF is set as 2.0.

245

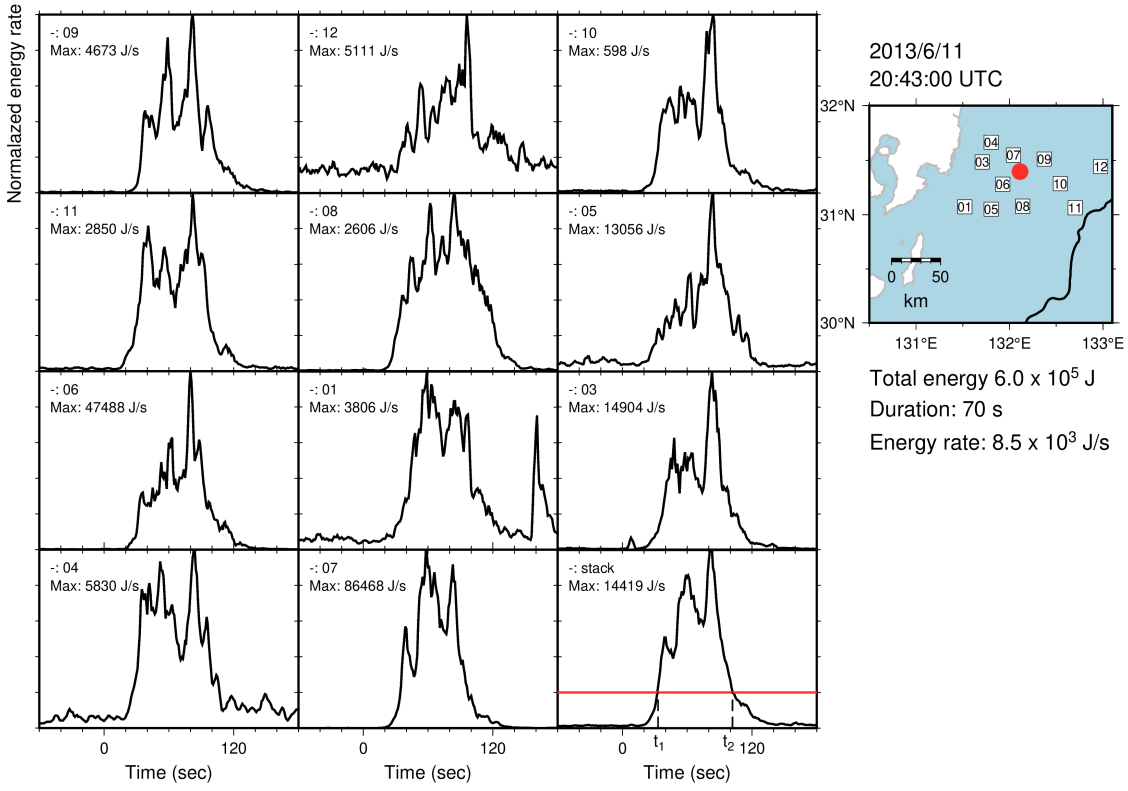

Figure 5. Temporal changes of energy rate functions of a tremor estimated at each OBS along with its stacked energy rate function. Red line of the stacked energy rate function indicates the threshold, which is set as 20% of the maximum value of the energy rate function. Red circle, squares and black line are the same as displayed in Fig. 3. Energy rate functions estimated from each station is arranged by azimuth clockwise from north.

253 **2.2. Estimation of moments of VLFEs**

254 We estimated the source durations and seismic moments of VLFEs temporally
255 corresponding to the tremors in 2013 and 2015 detected by Yamashita et al. (2015; 2021)
256 independently of tremor analysis. These values were evaluated by comparing observed and
257 synthetic waveforms following the procedure of Yabe et al. (2021) and Baba et al. (2021). We
258 additionally estimated the source durations and seismic moments of VLFEs in 2010 detected by
259 Asano et al. (2015) using the same method. As long-period VLFE signals are difficult to recognize
260 in short-period OBS records, we utilized continuous seismograms at onshore broadband F-net
261 stations for estimation. Before the analysis, we removed the instrumental responses, resampled at
262 one sample per second, and applied a bandpass filter in a frequency range of 0.02–0.05 Hz to
263 enhance the VLFE signals.

264 To reduce the computational costs of calculating Green's functions, reciprocal
265 calculations were conducted using OpenSWPC (Maeda *et al.* 2017). We set source grids at an
266 interval of 0.05º on the JIVSM plate boundary model of the area where tremors were detected
267 (Fig. 6a). The hypocentre of each VLFE was assumed to be at the nearest grid from the hypocentre
268 of the tremor located by Yamashita et al. (2015; 2021) or at the hypocentre of VLFEs located by
269 Asano et al. (2015). To calculate Green's functions, we used a three-dimensional velocity
270 structure model, JIVSM. For the density and quality factors, the values of JIVSM were used. A
271 frequency-independent model was adopted when calculating Green's functions. The minimum *S*-
272 wave velocity in the elastic volume was set as 1.5 km/s. The model includes topography
273 (ETOPO1; Amante & Eakins 2009), air, and seawater layers. The default values of OpenSWPC
274 were used for the density, seismic velocities, and quality factors in seawater and air. The model
275 volume was discretized using a uniform grid of 0.2 km. The focal mechanisms were assumed to
276 be consistent with the geometry of the plate boundary model of JIVSM and the plate convergence
277 direction of the plate motion model NUVEL-1A (DeMets *et al.* 1994). By combining the assumed
278 focal mechanisms and simulated Green's functions, we prepared a series of synthetic velocity
279 seismograms with triangular functions and source durations of 10–50 s (e.g., Takemura et al.,
280 2019).

281 We calculated the station- and component-averaged CCs between the synthetic and
282 observed waveforms. The time window of synthetic waveform is 150 s from the assumed origin
283 time of a VLFE. The origin time was searched for in the range from 30 s before to 30 s after the
284 start time of the duration range of each tremor located by Yamashita et al. (2015; 2021) and the
285 origin time of each VLFE located by Asano et al. (2015). The combination of source duration and
286 origin time, with the highest average CC in the grid search, was adopted. The dominant range of
287 source duration of VLFEs is 20–35 s. For tremor episodes in 2013 and 2015, if the highest
288 averaged CC is larger than 0.3, we regard that a VLFE occurs temporally corresponding to the

tremor. The difference of origin times between a VLFE and the corresponding tremor is in the range of ±20 s. For VLFE episode in 2010, events with average CCs smaller than 0.3 were discarded. We calculated the relative amplitudes by minimizing the variance reduction between observed and simulated waveforms with the source duration of the highest average CC (Baba et al. 2021; Yabe et al. 2021). We further estimated the seismic moments of VLFEs by multiplying the seismic moments of the synthetic waveform by estimated relative amplitudes. The moment, duration, and average CC of the example in Fig. 6 were 2.0×10^{15} Nm, 24 s, and 0.65, respectively. The seismic moment rate of the VLFE was obtained by dividing the seismic moment by the source duration which was estimated by the grid search based on CC between synthetic and observed waveforms.

We estimated the uncertainties of the VLFE moments by using the nonparametric bootstrap method. First, 100 bootstrap samples were prepared for each event. Since seven components are used for VLFE analysis (vertical component of N.KYKF and radial and vertical components in other F-net stations shown in Fig. 6), a bootstrap sample consisted of seven components including duplicates. Subsequently, VLFE moments were calculated by using each bootstrap sample composed of seven components. Then, we estimated the standard deviations of the 100 VLFE moments. The uncertainty of VLFE moments is 0.2–0.3 order (Fig. S3b).

The fit between the observed and simulated Love waves was not sufficient compared with that between observed and simulated Rayleigh wave (Fig. 6b). It may be inferred that the sedimentary structure of JIVSM at very shallow depths (< 5 km) in Hyuga-nada is insufficient to simulate Love waves, which are sensitive to shallow structures. We verified that the CCs between the simulated and observed waveforms of a regular earthquake located by Takemura et al. (2020) in the transverse components were also low, whereas those in the vertical and radial components were high (Fig. S5). Therefore, we used only the vertical and radial components (Rayleigh waves) when calculating the CCs. For the N.KYKF station, only the vertical component was utilized because the horizontal components were noisy.

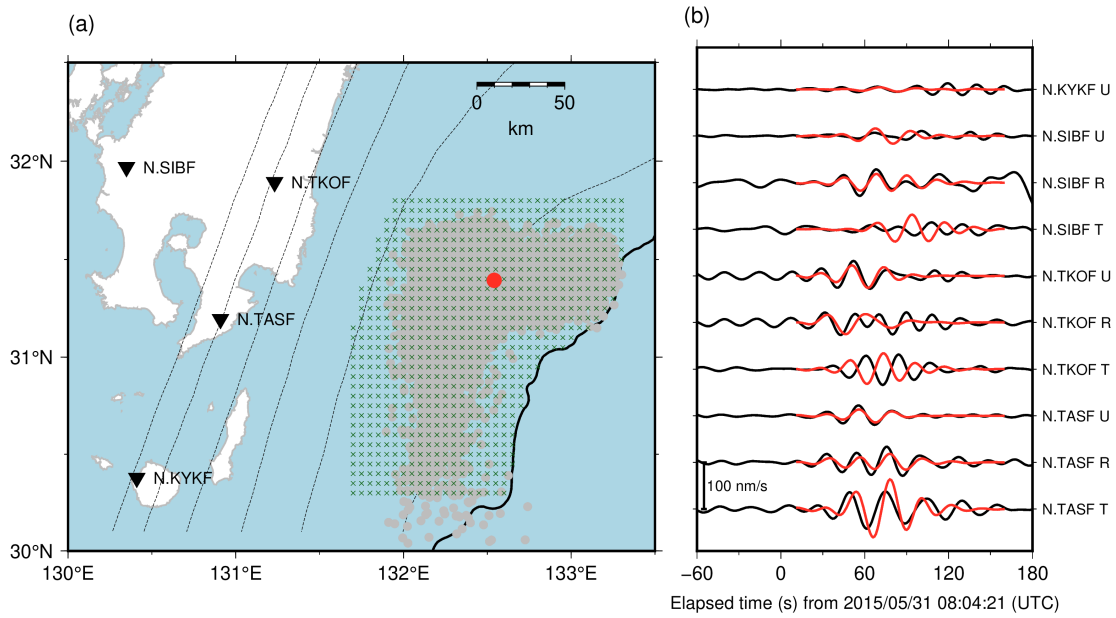

316

317 **Figure 6.** (a) VLFE source grids for the VLFE analysis. Crosses indicate the locations of the
318 VLFE source grids. Gray dots indicate the epicentres of tremors detected by Yamashita et al.
319 (2015; 2021). Red circle indicates the epicentre of the event displayed in Fig. 6b. Dashed contours
320 indicate the isodepth of the top of the Philippine Sea plate at 10-km intervals (JIVSM; Koketsu
321 et al. 2012). Black line represents the trench axis. Inverted triangles display the locations of the
322 F-net stations. (b) An example of a VLFE in a frequency range of 0.02–0.05 Hz. Waveforms are
323 depicted from 08:04:21 (UTC), May 31, 2015. Black and red lines are the observed and the
324 simulated waveforms, respectively. R, T, and U components represent the radial, transverse, and
325 vertical components, respectively.

326

3. Results

We estimated the energies of 1,672 and 6,126 shallow tremors in 2013 and 2015, respectively. We classified the analysis region into three areas based on spatial variation in energies of tremors and moments of VLFEs (Figs 7 and S6): Area A, south of 31.0º N; Area B, west of 132.4ºE, north of 31.0º N; and Area C, east of 132.4ºE, north of 31.0º N (see rectangles of Fig. 7). Area A is south of the subducted Kyushu-Palau Ridge, Area B is near the top of the subducted ridge, and Area C is east of the subducted ridge. Most of Areas A and C are outside the subducted ridge. In 2013, tremors and VLFEs occurred mainly in Areas A and B, whereas in 2015, they occurred mainly in Areas B and C. The dominant range of tremor energies was $10^{3.5}$–$10^{7.5}$ J with spatial variation (Fig. 7ac). In 2013 (Fig. 7a), tremors with higher energies (> 10^{6} J) were concentrated in Area A. This characteristic is confirmed in the maximum and median values of tremor energies (Fig. S6a). In 2015 (Fig. 7c), tremors with higher energies (> $10^{6.5}$ J) occurred near the north-eastern edge of the subducted Kyushu-Palau Ridge in Area C. The tremor energies near the trench axis in Area C were lower. These characteristics are also shown in the maximum tremor energies (Fig. S6b). Although median tremor energies are low in the longitude of 132.5º–132.7º due to the detection of many small events, the north-eastern edge of the subducted Kyushu-Palau Ridge in Area C is considered as high tremor energy area.

The moments were also estimated for 1,297, 904, and 1,785 shallow VLFEs in 2010, 2013, and 2015, respectively. The dominant range of the VLFE moments was $10^{13.5}$–$10^{16.5}$ Nm (Fig. 7b, d,e, and f). South of 31.0º N (Area A), VLFEs with higher moments (> $10^{15.5}$ Nm) occurred in 2010 and 2013 (Fig. 7be). North of 31.0º N, VLFEs extended near the trench axis in 2010 and 2015. In particular, VLFEs with higher moments (> $10^{15.5}$ Nm) in 2010 and 2015 (Figs 7de) are concentrated in Area C. In Area B, the VLFE moments are relatively low. These observations are stably confirmed in the maximum and median values of VLFE moments (Fig. S6c-f). The spatial variations in the VLFE moments and tremor energies for each observation period were similar (Fig. 7). The change in the maximum range of tremor energy or VLFE moment between Areas A and C and Area B is approximately one order (Fig. 7). Considering the uncertainty of tremor energies (0.5–1orders) and VLFE moments (0.2–0.3 orders), the spatial variation in tremor energy and VLFE moment is considered to be real. The spatial variations in the energy rates of tremors and moment rates of VLFEs were also approximately one order higher in Areas A and C than in Area B (Fig. S7). We summarized our observations: the energies of the tremors and moments of VLFEs are generally higher outside the subducted ridge (Areas A and C) than near the top of the subducted ridge (Area B).

The spatiotemporal variation in moments and energies of slow earthquakes and the change in the migration speed are associated (Fig. 8a and b). Hereafter, we mainly discuss the spatiotemporal variation in slow earthquakes based on VLFE activity because the spatiotemporal

variations in VLFE moments and tremor energies were similar, and the VLFE analysis covered all episodes in 2010, 2013, and 2015. Here, we summarized migration patterns in each episode. Their detailed features were described in the previous studies (Asano et al. 2015; Yamashita et al. 2015; Yamashita et al. 2021). The episodes in 2010 and 2015 are divided into three migrations and the 2013 episode is divided into two migrations (Figs. S8–S15 and Table S1). The 2010a, 2013a, and 2013b migrations were northward along the strike, whereas the 2010b, 2010c, 2015a, 2015b, and 2015c migrations were along the dip with various directions (Figs 8 and S8–S15; Table S1). All migrations along the strike direction consistently started in Area A (Figs 8b, S8, S11, and S12). Subsequently, the VLFEs migrated northward and entered the subducted ridge. After VLFEs entered Area B, their migration speed became slow (Fig. 8a and b). The spatiotemporal variation in the migration front seems to be parabolic (discussed in detail in Section 4.1). Rapid tremor reversals (RTRs; red dotted arrows in Figs 8b and S11), which is a fast backward migration (e.g., Houston et al. 2011), occurred during the migration in 2013.

In the main front of along-strike migrations, the moments of VLFEs became lower and the migration speed slowed after the front entered the Area B (Figs 8b, S8, S11, and S12). Therefore, the migration speed and the moments of VLFEs are positively correlated. On the other hand, the moments of the VLFEs in RTRs became higher when RTRs entered Area A (Figs 8b and S11). This suggests that the moments of VLFEs depend on the location.

In the downdip of shallow tremors and VLFEs, repeating earthquakes occurred at depths of 15–30 km (Fig. 9). The repeating earthquake activity manifests that the plate boundary around its patch is creeping; therefore, the large slip rate by repeating earthquakes suggests that the interplate coupling is weak (e.g., Uchida & Matsuzawa 2011). Fig. 9 compares the spatial distributions of slip rates from repeating earthquakes and cumulative moments of VLFEs. Cumulative moments of VLFEs may be also linked with the strength of interplate coupling (Baba *et al.* 2020). The interplate slip rate estimated from repeating earthquakes was higher in the south along the strike direction (Yamashita et al. 2012); therefore, the interplate coupling may be weaker at depths of 15–30 km in the south (downdip part of Area A) than in the north (downdip of Area B). The cumulative moment of shallow VLFEs in 2010 and 2013, episodes with along-strike migrations, was also lower in Area B than in Area A during the episodes (Fig. 9). Baba et al. (2020) found the tendency that cumulative moment of shallow VLFEs was higher in areas with weak interplate coupling along the Nankai Trough. In Hyuga-nada, the slip rate of repeating earthquakes and the cumulative moment of VLFEs are higher in the south (in and downdip of Area A) than in the north (in and downdip of Area B). These observations suggest that although there is a difference in the slip behaviour along the dip direction, such as repeating earthquakes and VLFEs, the interplate coupling may be consistently weak in the south along the strike direction. Although Area C is the northern part of Hyuga-nada, the cumulative moment of VLFEs

is high. Area C is apart from the repeating earthquake area and close to the trench axis unlike Areas A and B; therefore, interplate coupling may be different from Area B.

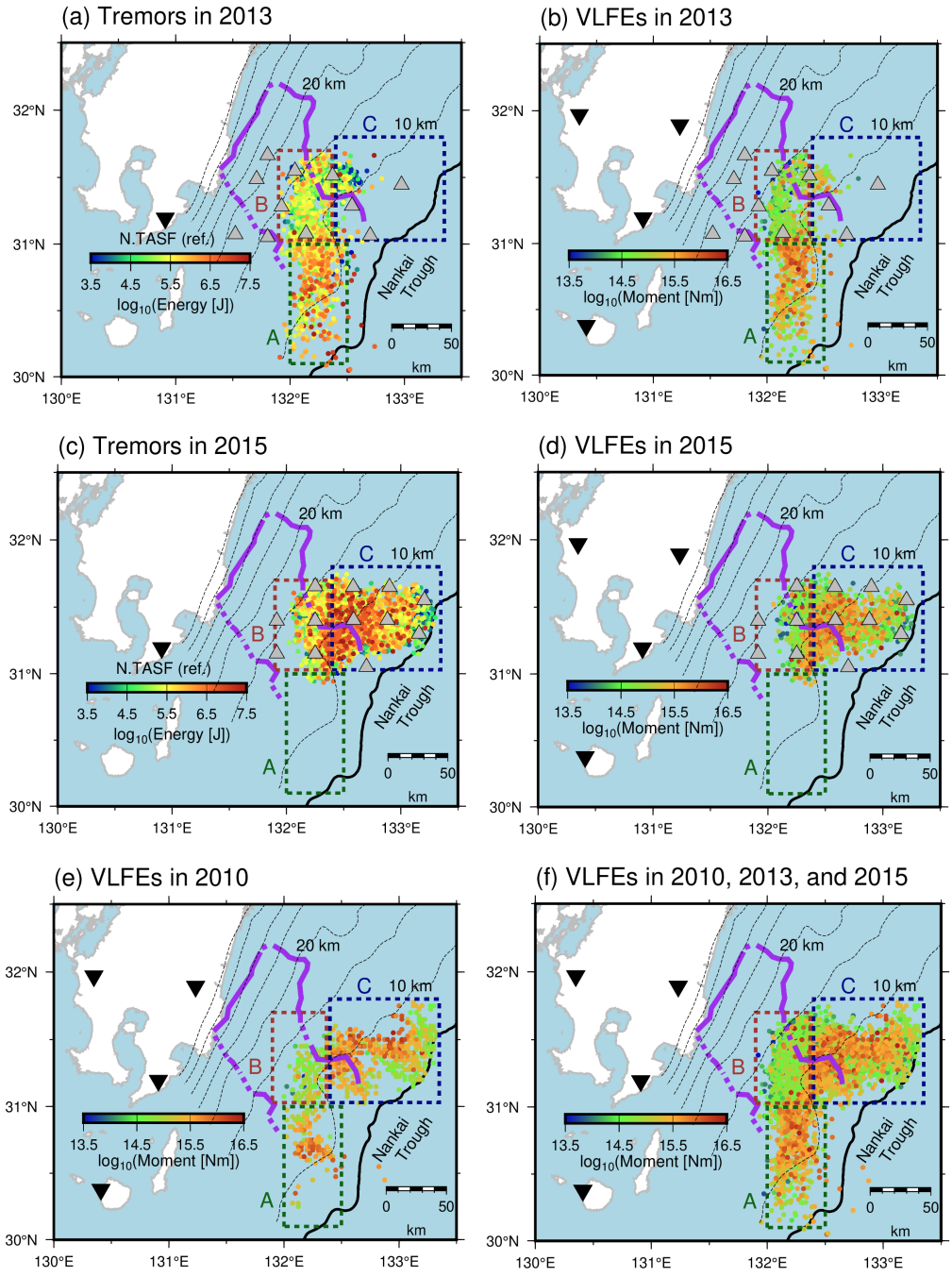

Figure 7. Spatial distribution of (a) energies of tremors in 2013, (b) moments of VLFEs in 2013, (c) energies of tremors in 2015, (d) moments of VLFEs in 2015, (e) moments of VLFEs in 2010, and (f) moments of VLFEs in all analysis periods. Green, brown, and dark blue dotted rectangles indicate the ranges of Area A, B, and C, respectively. Purple lines represent the inferred subducted

Kyushu-Palau Ridge (Yamamoto *et al.* 2013). Gray triangles depict the locations of OBSs. Black line represents the trench axis. Inverted triangles display the locations of the F-net stations. Dashed contours indicate the isodepth at the top of the Philippine Sea plate in intervals of 5 km (Nakanishi *et al.* 2018).

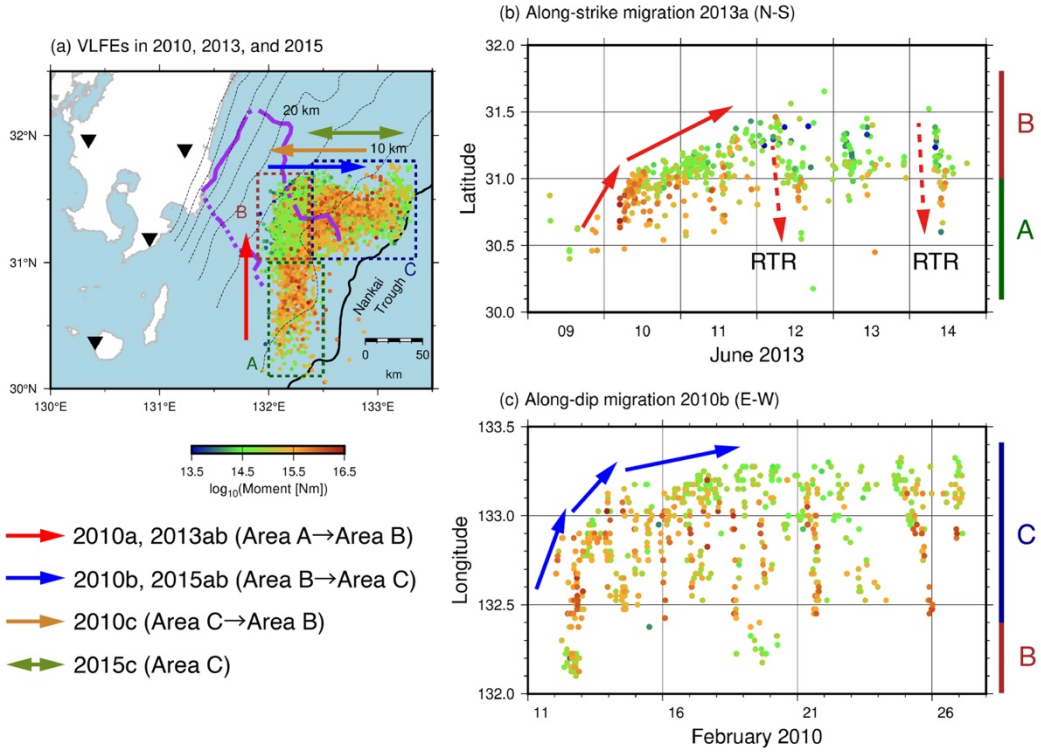

Figure 8. (a) Summary of slow earthquake migration patterns. Coloured arrows represent the direction of migration patterns. Coloured dotted rectangles, dashed contours, purple lines and black inverted triangles are the same as displayed in Fig. 7. (b and c) Spatiotemporal distributions of (b) the along-strike migration 2013a and (c) the along-dip migration 2010b with moments of VLFEs. Coloured arrows indicate the direction of migrations. Red dotted arrows in Fig. 8b represents the RTR.

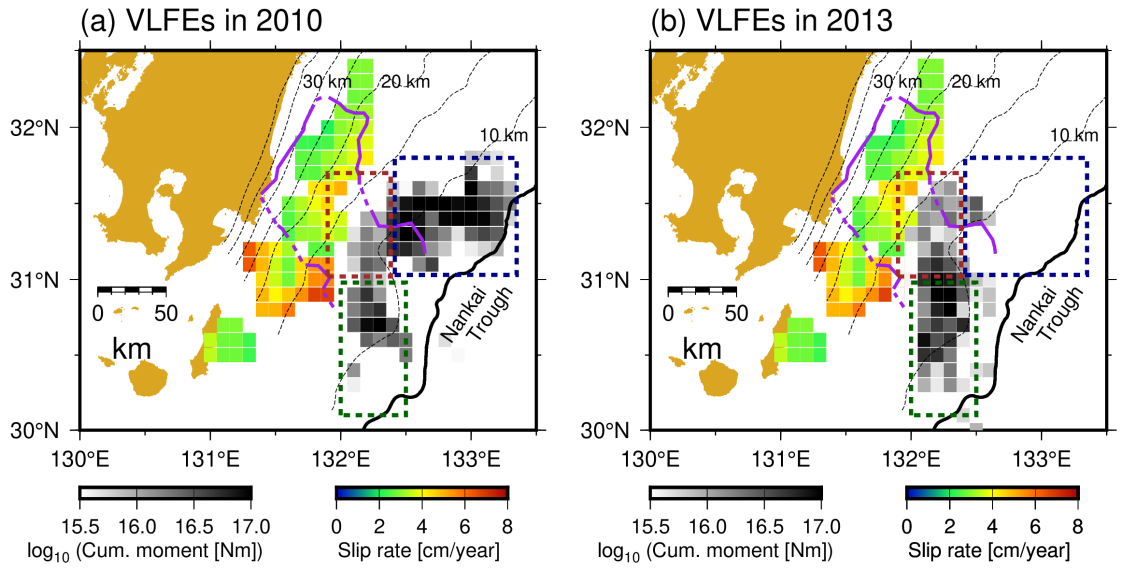

421

422 **Figure 9.** Relationship between slip rates estimated from repeating earthquakes (Yamashita et al.
423 2012) and shallow slow earthquakes. Gray scales exhibit the cumulative moments of VLFEs.
424 Colour scale indicates the slip rate estimated from repeating earthquakes. Coloured dotted
425 rectangles, purple lines, black lines, and dashed contours are the same as in Fig. 7.

426

427

4. Discussion

4.1. Along-strike spatial variation in slow earthquake activity

To investigate the controlling factor of the along-strike variation in slow earthquake activity in Hyuga-nada, we compared the activity with a physical model of along-strike slow earthquake migration by Ando et al. (2012). In their model, high- and low-strength brittle tremor patches exist on the ductile background based on Newtonian rheology. The rupture of these brittle patches is triggered by the stress increase at the migration front of an SSE. They predicted that tremors start migrating energetically in areas with high tremor-patch strength (strong patch areas) and decelerates with a parabolic spatiotemporal pattern in areas with low tremor-patch strength (weak patch areas). In Hyuga-nada, the migration speed was faster, and the VLFE moment was higher in Area A than in Area B (Fig. 8). These observations are consistent with the modelling results by Ando et al. (2012). The along-strike variation in slow earthquake activity in Hyuga-nada can be explained by the difference in the patch strength of slow earthquakes, where Areas A and B are considered strong and weak patch areas, respectively (Fig. 10).

The spatial variations in tremor activity in Shikoku and VLFE activity off the south-eastern Kii Peninsula were also discussed based on Ando et al. (2012) (Shikoku: Kano et al. 2018b; off the southeast Kii Peninsula: Yamamoto et al. 2022). In Shikoku, western and central Shikoku were interpreted as strong and weak patch areas, respectively, whereas the areas west of and inside the subducted Paleo-Zenisu ridge off the Kii Peninsula were regarded as strong and weak patch areas, respectively.

A possible factor for the along-strike spatial variation in slow earthquake activity in Hyuga-nada is the spatial heterogeneity of pore fluid pressure. Kano et al. (2018b) suggested that the heterogeneity of strong and weak patch areas is caused by the variation in effective normal stress, which is associated with that in the fluid pressure on the plate boundary. Takemura et al. (2022a) discussed that the variation in the pore fluid pressure can induce the change of the migration speed, which can be considered as a proxy for rupture propagation of an SSE (e.g., Bartlow et al. 2011; Ito et al. 2007), off the Cape Muroto and Kii Peninsula. In Hyuga-nada, the change in migration speed between Area A and B may be caused by the pore fluid pressure heterogeneity. To discuss the variation in the pore fluid pressure in Hyuga-nada in more detail, investigations of seismic velocity structures (especially V_S and V_P/V_S ratio) are required in future work.

Another possible factor is the geometrical effects of the subduction of a ridge. Wang and Bilek (2011) suggested that a fracture network caused by a subducted seamount generates structural and stress heterogeneities. According to Chesley et al. (2021), the subduction of a seamount can transport a considerable volume of fluid to the forearc and create a fluid-rich fracture zone, which can change the effective normal stress around the plate boundary. Takemura

et al. (2022b) and Yamamoto et al. (2022) suggested the variation in cumulative moments of VLFEs which is associated with subducted Paleo-Zenisu ridge off the Kii Peninsula. In Hyuga-nada, the subduction of the Kyushu-Palau ridge may also generate the stress heterogeneity on the plate boundary.

As mentioned in Section 3, the spatiotemporal variation in the migration front appears to be parabolic. Following Ando et al. (2012), we investigated which function is better for fitting the migration front in 2013a, exponential ($t = C\ exp\big(a(x + x_1)\big) + t_1$; t is the elapsed time, x is the migration distance, C, a , x_1, and t_1 are constant) or parabolic ($t = D^{-1}(x + x_2)^2 + t_2$; D is the diffusion coefficient, x_2 and t_2 are constant). Although tremor epicentres were scattered around the start of migration, the migration pattern seems to be better fitted by a parabola (Fig. 11) rather than exponential, and the diffusion coefficient D is evaluated as ~6×10^4 m^2/s (Fig. S16).

Ando et al. (2012) assumed that fault strength is equals to τ_p when slip velocity v=0 and equals to $\tau_r+\eta v$ when v>0 following Ando et al. (2010) and Nakata et al. (2011). τ_p, τ_r, η are peak strength, residual strength, and viscosity factor, respectively. In Ando et al. (2012), τ_r is set as zero and the patch strength is represented by τ_p. The difference in τ_p between strong and weak patches is supposed to be represented by that in stress drop. Therefore, we roughly evaluated the variation in the stress drop of the VLFEs in Hyuga-nada. Assuming a circular crack model, the seismic moment M_0 of an earthquake is given by (e.g., Kanamori & Anderson 1975):

$$M_0 = \frac{16}{7}\Delta\tau r^3 \quad (5)$$

where $\Delta\tau$ is the stress drop and r is the radius of the patch. In this section, this relationship is further assumed in VLFEs. The median moment of a VLFE in Area A (strong patch area) and in Area B (weak patch area) is (2.2±1.2)×10^{15} Nm and (6.5±4.1)×10^{14} Nm, respectively (Fig. 7b, d, e, and f). Considering that Ohta & Ide (2017) estimated the source radius of a deep VLFE with M_0=1.2×10^{14} Nm as ~5 km, we assume the radius of a shallow VLFE patch in Hyuga-nada with M_0=$10^{13.5}$–$10^{16.5}$ Nm (Figs. 7b, d, e, f, S6c, and S6e) as 3–30 km. If patches with a radius r of 3–30 km are assumed, the median stress drop of a VLFE in Areas A and B is evaluated as 3.6×10^1–3.6×10^4 Pa and 1.1×10^1–1.1×10^4 Pa, respectively. The spatiotemporal distribution of migration is parabolic if the difference in stress drop between strong and weak patches is sufficient (Ando et al. 2012). As indicated by the fitting of the migration front, the spatiotemporal variation in the slow earthquake migration front was parabolic (Figs. 8b and 11). Although the model of Ando et al. (2012) assumed an 11-times differences between strong and weak patches, if the patch size in Areas A and B is similar, parabolic migration pattern was observed by an approximately three-time difference in the stress drops of these patches in Hyuga-nada. On the other hand, since the difference in the moment of VLFEs between Areas A and B may be due to the patch size, slip distribution of VLFEs should be investigated in future studies. However, the estimation of slip

areas of shallow VLFEs is a challenging issue due to offshore heterogeneities along the propagation path. The patch heterogeneity may be a key factor of variations in tremor energy, VLFE moment, and migration speed in Hyuga-nada. Although we conducted a general classification of slow earthquake areas, more statistical approaches, such as clustering procedures, may be useful to construct a new model of slow earthquake activity.

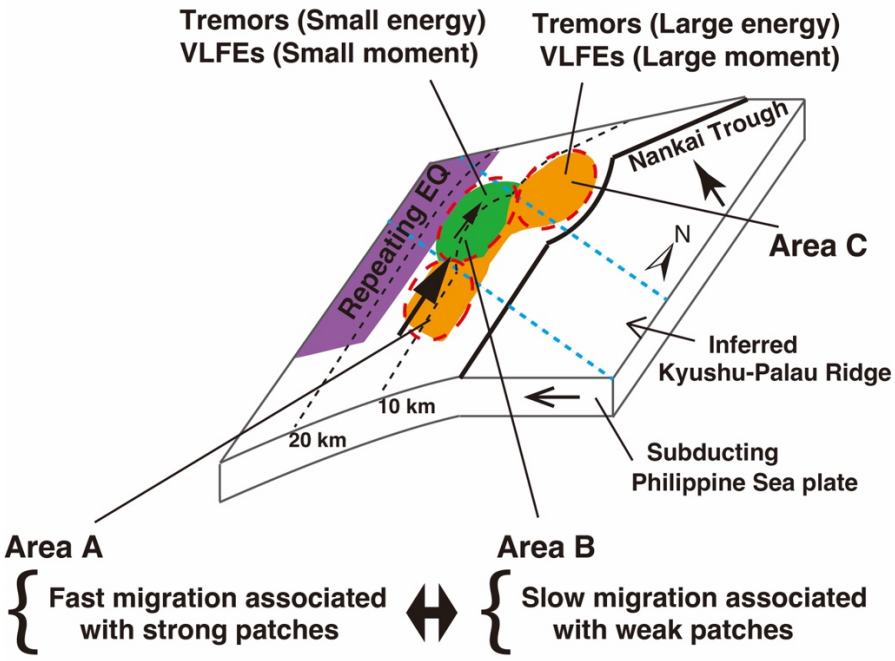

Figure 10. Schematic illustration of the interpretation of distributions of slow earthquakes and Kyushu-Palau Ridge.

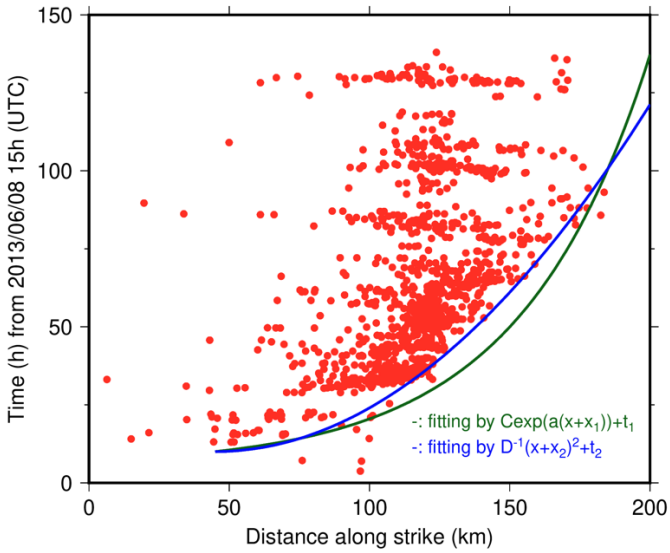

512

513 **Figure 11.** Spatiotemporal distribution of tremor migration in the episode of 2013a. Vertical and
514 horizontal axis shows the elapsed time from 2013/06/08 15:00:00 (UTC) and distance along the
515 strike (N-S) from 30.0ºN, respectively. Blue and green lines indicate the parabolic and exponential
516 curves, respectively.

517

4.2. Scaled energy of shallow slow earthquakes in Hyuga-nada

To discuss the characteristics of the source process of slow earthquakes in Hyuga-nada, we estimated the scaled energy following previous studies (e.g., Ide et al., 2008; Yabe et al., 2019; 2021) using the ratio between the tremor energy rate and VLFE moment rate for activities in 2013 and 2015, when the energy rate could be estimated from the OBS records. The dominant range of the scaled energy was $10^{-11.5}$–$10^{-8.5}$ both in 2013 and 2015 (Fig. 12ab). Dominant ranges of scaled energies did not change significantly between episodes in 2013 and 2015 (Fig. S17). The range of the median scaled energy is in the range of $10^{-10.5}$–$10^{-9.5}$ in all areas (Fig. 12cd). The median scaled energy is approximately 0.5 orders smaller around the eastern edge of the Kyushu-Palau Ridge in Area C than in other areas. However, the variation in scaled energy is ranged to three to four orders in all areas (Fig. S17). In addition, the uncertainty of scaled energy often reaches approximately one order (Fig. S18). Therefore, it is difficult to consider that the 0.5 orders difference in median scaled energy in the western part of Area C is due to the variation in the rupture process in Hyuga-nada. The characteristics of the scaled energy do not change in spatially and temporally in the order scale inside the Hyuga-nada. Apparent stress is estimated by multiplying scaled energy by rigidity. Since the range of scaled energy is similar between Areas A and B, the apparent stress is similar if the rigidity is the same.

The range of scaled energies in Hyuga-nada is similar to or one order smaller compared to the off the Cape Muroto and Kii Peninsula (10^{-10}–10^{-8}; Yabe et al. 2021, 2019), along the Japan Trench (10^{-10}–10^{-9}; Yabe et al. 2021), and in Costa Rica (10^{-9}–10^{-8}; Baba et al. 2021). The range of scaled energies of shallow slow earthquakes in Hyuga-nada is also similar to those of deep slow earthquakes in southwest Japan, Cascadia, and Mexico ($10^{-9.5}$–10^{-9}; Ide, 2016; Ide and Maury, 2018; Ide and Yabe, 2014; Fig. 13). However, the range of scaled energy in Hyuga-nada is broader than other slow earthquake regions.

Ide (2008) and Ide & Maury (2018) discussed the theoretical relationship between seismic energy rate and seismic moment rate of slow earthquakes by the Brownian slow earthquake model. In their model, the characteristic size of the slip area S is described by:

$$S = Cr^2 \qquad (6)$$

where r is a random variable and C is a constant. The temporal change of r is described by:

$$dr = -\alpha r dt + \sigma dB \qquad (7)$$

where α is the characteristic frequency of slow earthquakes (α^{-1} is a characteristic time), dB is the random variable of Gaussian distribution with the mean 0 and the variance 1, σ is the fluctuation magnitude. They discussed that the energy rate divided by the square of the moment rate depends on a characteristic frequency of a slow earthquake event, α:

$$\frac{E[E_{rate}]}{E[M_{rate}]^2} = \frac{4\alpha}{5\pi\rho {V_s}^5 \Delta t} \qquad (8)$$

where ρ is the density, V_s is the *S*-wave velocity, and Δt is the time steps of the stochastic process. E[E_{rate}] and E[M_{rate}] indicates the long-term averages of energy rates and moment rates, respectively. Ide & Maury (2018) evaluated E[E_{rate}]/E[M_{rate}]^2 and α^{-1} of seismic slow earthquakes in deep southwest Japan, Cascadia, and Mexico as 10^{-22}–10^{-20} and 0.3–30 s, respectively. The range of α^{-1} of the SSE scale in deep southwest Japan, Cascadia, and Mexico evaluated by Ide & Maury (2018) is 75–300 s. E[E_{rate}]/E[M_{rate}]^2 in Hyuga-nada is estimated to be 10^{-25}–$10^{-21.5}$ (Fig. S19). The small value of E[E_{rate}]/E[M_{rate}]^2 may be caused by small ρ and/or V_s in Hyuga-nada. However, if ρ, V_s, and Δt is the same order as in the values of Ide & Maury (2018), α^{-1} in Hyuga-nada is estimated to be 10–30000 s. In Hyuga-nada, there may be slow earthquake events that have similar or longer characteristic times than those of other slow earthquake regions. In addition, the range of the characteristic time is broader in Hyuga-nada than in other slow earthquake regions; therefore, slow earthquakes in Hyuga-nada may have various spectral features. Based on Ide & Maury (2018), the wide range of characteristic time in this area suggests width variations of tremor source area.

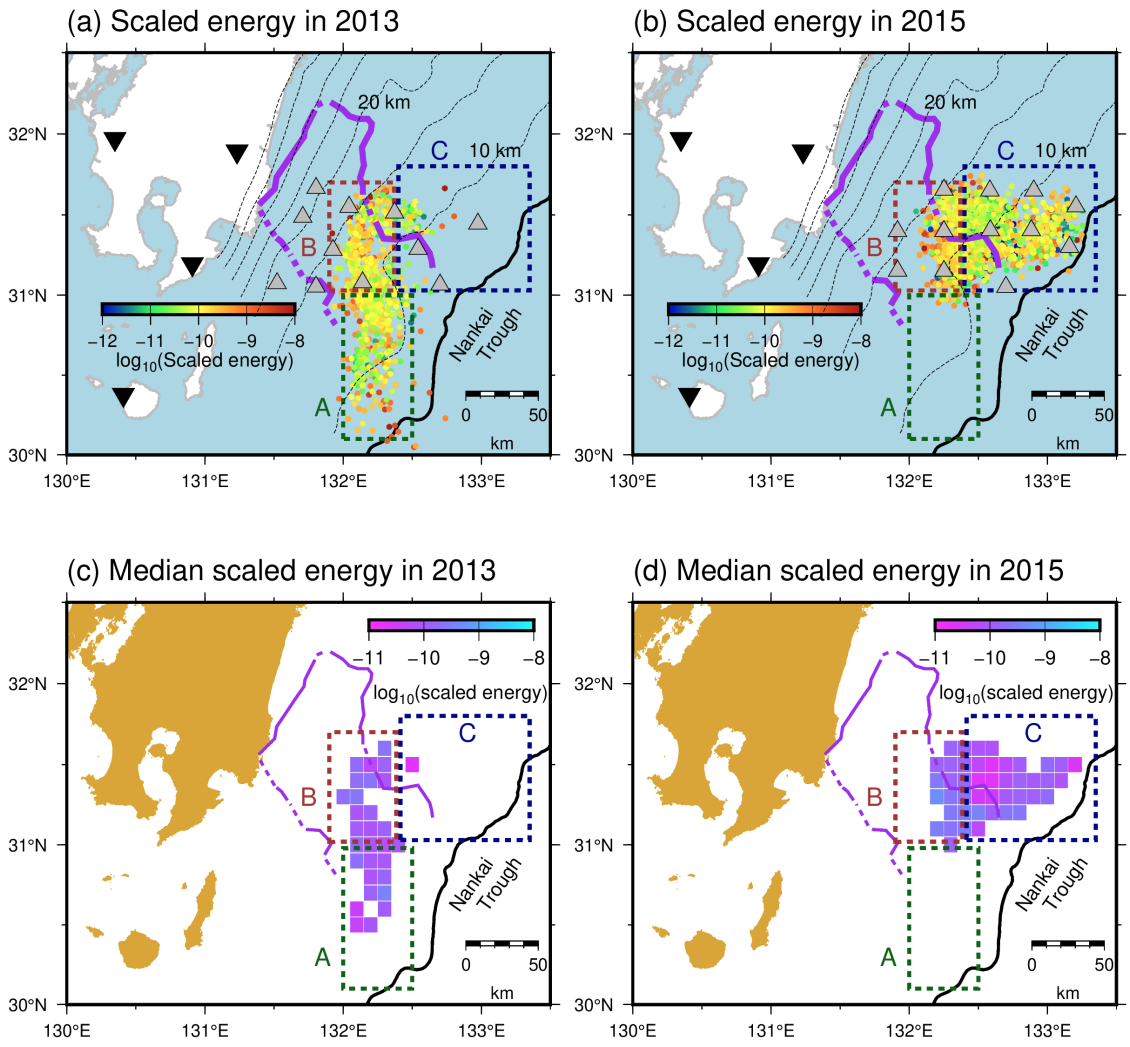

Figure 12. Spatial distribution of scaled energy of shallow slow earthquakes (a) in 2013 and (b) in 2015. Spatial distribution of the median scaled energy in the grid of 0.1° × 0.1° where the number of events is larger than 10 (c) in 2013 and (d) in 2015. Coloured dotted rectangles, purple lines, black lines, gray triangles, inverted triangles, and dashed contours are the same as in Fig. 7.

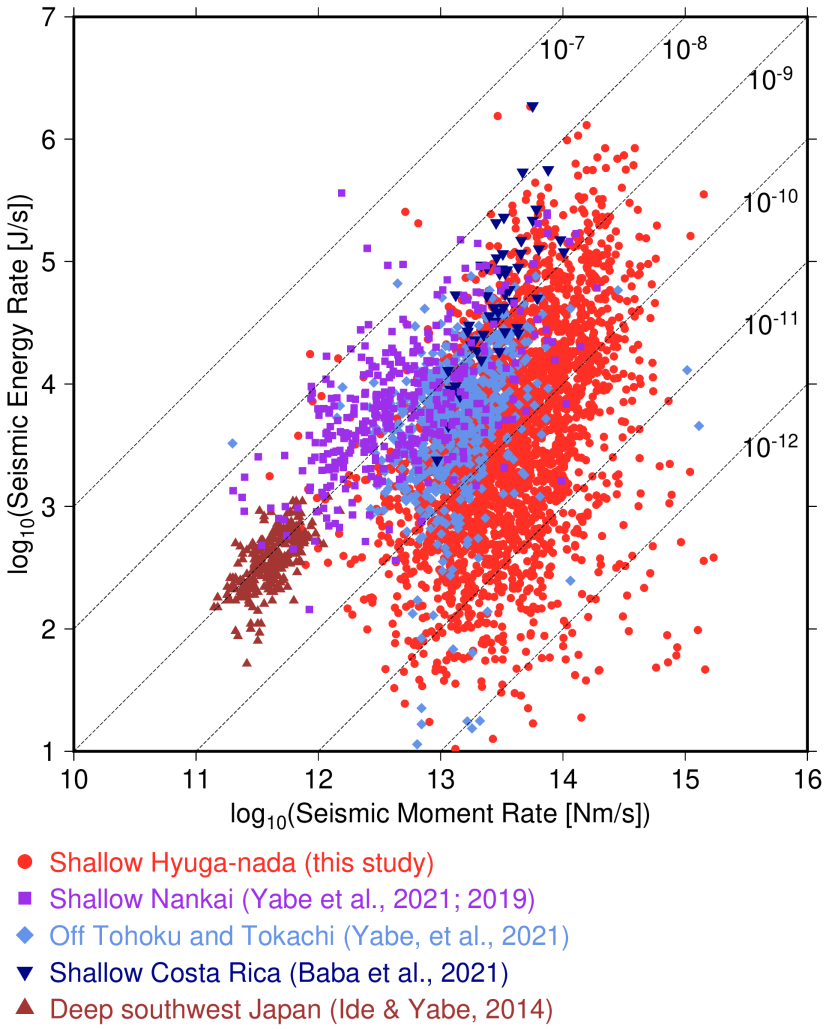

575

576 **Figure 13.** Relationship between seismic moment rates of VLFEs and seismic energy rates of
577 tremors. Red circles, purple squares, green diamonds, dark blue inverted triangles, and dark blue
578 triangles indicate the relationships between seismic moment rates of VLFEs and seismic moment
579 rates of tremors in shallow Hyuga-nada (this study), shallow Nankai except Hyuga-nada (Yabe *et*
580 *al.* 2019, 2021), off Tohoku and Tokachi (Yabe *et al.* 2021), shallow Costa Rica (Baba *et al.* 2021),
581 and deep slow earthquakes (Ide & Yabe 2014; Ide 2016; Ide & Maury 2018). Dashed lines
582 represent scaled energies of 10^{-7}, 10^{-8}, 10^{-9}, 10^{-10}, 10^{-11}, and 10^{-12}.
583
584

5. Conclusion

To investigate the spatial variation in the source characteristics of shallow slow earthquakes in Hyuga-nada at a higher resolution, we estimated the energies of shallow tremors, moments of shallow VLFEs, and the scaled energy of shallow slow earthquakes in Hyuga-nada using the data from permanent onshore broadband and temporary offshore seismometers. The dominant ranges of energies of tremors and moments of VLFEs are $10^{3.5}$–$10^{7.5}$ J and $10^{13.5}$–$10^{16.5}$ Nm, respectively. The energies of tremors and moments of VLFEs are higher in Areas A and C (most of which are outside the subducted Kyushu-Palau Ridge) than in Area B (near the top of the subducted ridge). The migration of tremors and VLFEs along the strike direction started in Area A (south of the subducted ridge) with events of higher tremor energies and VLFE moments. After going north and entering Area B (near the top of the subducted ridge), the migration speed slowed, and the tremor energies and VLFE moments were observed to be low (Fig. 8b).

Based on the physical model of Ando et al. (2012), strengths of slow earthquake patches in Areas A and B are expected to be strong and weak, respectively. The spatiotemporal distribution of the tremor migration in 2013 is fitted by a parabolic function with the high energy and moment events at the initiation of the migration in Area A. If a circular crack model and same patch sizes are assumed, the difference in median stress drop of the VLFEs in Area A (strong patch) and Area B (weak patch) is evaluated as three times. This difference in the stress drop of strong and weak patches may generate a parabolic migration pattern. The along-strike variation in the rupture process on the plate boundary, such as the stress drop, in slow earthquake regions can cause variations in the moment of slow earthquakes and migration pattern near the southern edge of the subducted ridge.

The dominant range of scaled energy of slow earthquakes in Hyuga-nada is estimated as $10^{-11.5}$–$10^{-8.5}$. The range of scaled energies in Hyuga-nada is similar to or one order smaller than other slow earthquake regions. Inside the Hyuga-nada, the spatial variation in scaled energy is not found. Since the range of scaled energy is similar between Areas A and B, the apparent stress may be similar if the rigidity is the same. Furthermore, this range is broader than other regions. Based on the Brownian slow earthquake model by Ide & Maury (2018), the characteristic times of slow earthquakes in Hyuga-nada (10–30000 s) is similar to or longer than those of other slow earthquake regions (0.3–30 s). Following Ide & Maury (2018), the wide range of characteristic time suggests the width variations of slow earthquake source area in Hyuga-nada. The slow earthquakes in Hyuga-nada may have various spectral features.

Acknowledgements

We would like to thank the Editor Víctor M. Cruz-Atienza, the Assistant Editor Louise Alexander, and two anonymous reviewers for their valuable comments and suggestions. We thank Ryosuke Ando, Aitaro Kato, Satoshi Ide, Asuka Yamaguchi, Shoichi Yoshioka, Takashi Tonegawa, Ryuta Arai, Masaru Nakano, Takane Hori, Eiichiro Araki, and Yojiro Yamamoto for their valuable discussions. We appreciate Youichi Asano for providing the shallow VLFE data in 2010. This research was supported by the JSPS KAKENHI Grant in Science Research on Innovative Areas "Science of Slow Earthquakes" (JP16H06472), Grant-in-Aid for Scientific Research on Transformative Research Areas (A) "Science of Slow-to-Fast earthquakes" (JP21H05205), and JSPS Research Fellowship DC1 (JP19J20760). This study was also supported by the ERI JURP 2021-S-B102. This research is part of Satoru Baba's PhD thesis (Baba, 2022).

Author contribution statement

SB conducted analysis and drafted the manuscript. SB, ST, KO, TA, YY, and MS contributed the interpretation of this study. YY and MS designed the ocean bottom seismometer observation. All authors read and approved the manuscript.

Data availability statement

A part of OBS data for this study was acquired by "Research project for compound disaster mitigation on the great earthquakes and tsunamis around the Nankai Trough region," a project of the Ministry of Education, Culture, Sports, Science and Technology, Japan. The OBS data is available from the corresponding author upon request. We used the F-net broadband seismograms from the National Research Institute for Earth and Disaster Resilience (2019) and the earthquake catalogues from the Japan Meteorological Agency (https://www.data.jma.go.jp/svd/eqev/data/bulletin/index_e.html). OpenSWPC code Version 5.0.2 (Maeda *et al.* 2017) was utilized to calculate synthetic waveforms. We used the Fujitsu PRIMERGY CX600M1/CX1640M1 (Oakforest-PACS) at the Information Technology Center, the University of Tokyo for numerical simulations. Generic mapping tools (Wessel *et al.* 2013) and the Seismic Analysis Code (Helfrich et al., 2013) are used to prepare figures and process seismograms, respectively. Catalogues of shallow tremors detected by Yamashita et al. (2015; 2021) can be downloaded from the Slow Earthquake Database (Kano, et al. 2018a). The estimated tremor energies and VLFE moments are provided in an open access repository, zenodo (https://doi.org/10.5281/zenodo.8220097).

655 **References**

656 Amante, C., & Eakins, B.W. 2009. ETOPO1 1 Arc-Minute Global Relief Model: Procedures, Data
657 Sources and Analysis. NOAA Technical Memorandum NESDIS NGDC-24.
658 https://doi.org/10.7289/V5C8276M

659 Ando, R., Nakata, R. & Hori, T., 2010. A slip pulse model with fault heterogeneity for low-
660 frequency earthquakes and tremor along plate interfaces. *Geophys Res Lett*, **37**, 1–5.
661 doi:10.1029/2010GL043056

662 Ando, R., Takeda, N. & Yamashita, T., 2012. Propagation dynamics of seismic and aseismic slip
663 governed by fault heterogeneity and Newtonian rheology. *Journal of Geophysical Research*
664 *B: Solid Earth*, **117**, Blackwell Publishing Ltd. doi:10.1029/2012JB009532

665 Aoi, S., Asano, Y., Kunugi, T., Kimura, T., Uehira, K., Takahashi, N., Ueda, H., *et al.*, 2020.
666 MOWLAS: NIED observation network for earthquake, tsunami and volcano. *Earth, Planets*
667 *and Space*, **72**, Springer Berlin Heidelberg. doi:10.1186/s40623-020-01250-x

668 Asano, Y., Obara, K., Matsuzawa, T., Hirose, H. & Ito, Y., 2015. Possible shallow slow slip events
669 in Hyuga-nada, Nankai subduction zone, inferred from migration of very low frequency
670 earthquakes. *Geophys Res Lett*, **42**, 331–338. doi:10.1002/2014GL062165

671 Baba, S., 2022. Spatiotemporal characteristics of slow earthquakes in subduction zones around
672 Japan. PhD thesis of the University of Tokyo, Japan.

673 Baba, S., Obara, K., Takemura, S., Takeo, A. & Abers, G.A., 2021. Shallow Slow Earthquake
674 Episodes Near the Trench Axis Off Costa Rica. *J Geophys Res Solid Earth*.
675 doi:10.1029/2021JB021706

676 Baba, S., Takemura, S., Obara, K. & Noda, A., 2020. Slow Earthquakes Illuminating Interplate
677 Coupling Heterogeneities in Subduction Zones. *Geophys Res Lett*, **47**, 4–5.
678 doi:10.1029/2020GL088089

679 Bartlow, N.M., Miyazaki, S., Bradley, A.M. & Segall, P., 2011. Space-time correlation of slip and
680 tremor during the 2009 Cascadia slow slip event. *Geophys Res Lett*, **38**, Blackwell
681 Publishing Ltd. doi:10.1029/2011GL048714

682 Chesley, C., Naif, S., Key, K. & Bassett, D., 2021. Fluid-rich subducting topography generates
683 anomalous forearc porosity. *Nature*, **595**, 255–260, Nature Research. doi:10.1038/s41586-
684 021-03619-8

685 DeMets, C., Gordon, R.G., Argus, D.F. & Stein, S., 1994. Effect of recent revisions to the
686 geomagnetic reversal time scale on estimates of current plate motions. *Geophys Res Lett*,
687 **21**, 2191–2194. doi:10.1029/94GL02118

688 Dragert, H., Wang, K., James, T.S., 2001. A Silent Slip Event on the Deeper Cascadia Subduction
689 Interface. *Science (1979)*, **292**, 1525–1528. doi:10.1126/science.1060152

690 Helffrich, G., Wookey, J., & Bastow, I. 2013. The Seismic Analysis Code. Cambridge: Cambridge

University Press. doi:10.1017/CBO9781139547260

Hirose, H., Hirahara, K., Kimata, F., Fujii, N. & Miyazaki, S., 1999. A slow thrust slip event following the two 1996 Hyuganada earthquakes beneath the Bungo Channel, southwest Japan. *Geophys Res Lett*, **26**, 3237–3240. doi:10.1029/1999GL010999

Houston, H., Delbridge, B.G., Wech, A.G., & Creager, K.C. 2011. Rapid tremor reversals in Cascadia generated by a weakened plate interface. Nature Geoscience, 4, 404-409, doi:10.1038/NGE01157

Ide, S., 2016. Characteristics of slow earthquakes in the very low frequency band: Application to the Cascadia subduction zone. *J Geophys Res Solid Earth*, **121**, 5942–5952. doi:10.1002/2016JB013085

Ide, S. & Beroza, G.C., 2001. Does apparent stress vary with earthquake size? *Geophys Res Lett*, **28**, 3349–3352.

Ide, S. & Beroza, G.C., 2023. Slow earthquake scaling reconsidered as a boundary between distinct modes of rupture propagation. *Proc Natl Acad Sci U S A*, **120**, National Academy of Sciences. doi:10.1073/pnas.2222102120

Ide, S., Beroza, G.C., Shelly, D.R. & Uchide, T., 2007a. A scaling law for slow earthquakes. *Nature*, **447**, 76–79. doi:10.1038/nature05780

Ide, S., Imanishi, K., Yoshida, Y., Beroza, G.C. & Shelly, D.R., 2008. Bridging the gap between seismically and geodetically detected slow earthquakes. *Geophys Res Lett*, **35**, 2–7. doi:10.1029/2008GL034014

Ide, S. & Maury, J., 2018. Seismic Moment, Seismic Energy, and Source Duration of Slow Earthquakes: Application of Brownian slow earthquake model to three major subduction zones. *Geophys Res Lett*, **45**, 3059–3067. doi:10.1002/2018GL077461

Ide, S., Shelly, D.R. & Beroza, G.C., 2007b. Mechanism of deep low frequency earthquakes: Further evidence that deep non-volcanic tremor is generated by shear slip on the plate interface. *Geophys Res Lett*, **34**. doi:10.1029/2006GL028890

Ide, S. & Yabe, S., 2014. Universality of slow earthquakes in the very low frequency band. *Geophys Res Lett*, **41**, 2786–2793. doi:10.1002/2014GL059712

Igarashi, T., 2020. Catalog of small repeating earthquakes for the Japanese Islands. *Earth, Planets and Space*, **72**, Springer Berlin Heidelberg. doi:10.1186/s40623-020-01205-2

Ito, Y., Obara, K., Shiomi, K., Sekine, S. & Hirose, H., 2007. Slow Earthquakes Coincident with Episodic Tremors and Slow Slip Events. *Science (1979)*, **315**, 503–506. doi:10.1126/science.1134454

Kanamori, H. & Anderson, D.L., 1975. THEORETICAL BASIS OF SOME EMPIRICAL RELATIONS IN SEISMOLOGY. *Bulletin of the Seismological Society of America*, Vol. 65. Retrieved from http://pubs.geoscienceworld.org/ssa/bssa/article-

pdf/65/5/1073/5320189/bssa0650051073.pdf
Kanamori, H. & Rivera, L., 2006. Energy partitioning during an earthquake. *Geophysical Monograph Series*, **170**, 3–13. doi:10.1029/170GM03
Kaneko, L., Ide, S. & Nakano, M., 2018. Slow Earthquakes in the Microseism Frequency Band (0.1–1.0 Hz) off Kii Peninsula, Japan. *Geophys Res Lett*, **45**, 2618–2624. doi:10.1002/2017GL076773
Kano, M., Aso, N., Matsuzawa, T., Ide, S., Annoura, S., Arai, R., Baba, S., *et al.*, 2018a. Development of a Slow Earthquake Database. *Seismological Research Letters*, **89**, 1566–1575. doi:10.1785/0220180021
Kano, M., Kato, A., Ando, R. & Obara, K., 2018b. Strength of tremor patches along deep transition zone of a megathrust. *Sci Rep*, **8**, Nature Publishing Group. doi:10.1038/s41598-018-22048-8
Kato, A., Obara, K., Igarashi, T., Tsuruoka, H., Nakagawa, S. & Hirata, N., 2012. Propagation of Slow Slip Leading Up to the 2011 Mw 9.0 Tohoku-Oki Earthquake. *Science (1979)*, **335**, 705–708. doi:10.1126/science.1215141
Koketsu, K., Miyake, H., Suzuki, H., 2012. Japan Integrated Velocity Structure Model Version 1. In: Proceedings of the 15th World Conference on Earthquake Engineering, Lisbon, Portugal, 24-28 September, Paper 1773.
Maeda, T., Takemura, S. & Furumura, T., 2017. OpenSWPC: An open-source integrated parallel simulation code for modeling seismic wave propagation in 3D heterogeneous viscoelastic media 4. Seismology. *Earth, Planets and Space*, **69**, Springer Berlin Heidelberg. doi:10.1186/s40623-017-0687-2
Masuda, K., Ide, S., Ohta, K. & Matsuzawa, T., 2020. Bridging the gap between low-frequency and very-low-frequency earthquakes. *Earth, Planets and Space*, **72**, Springer Berlin Heidelberg. doi:10.1186/s40623-020-01172-8
Nadeau, R.M. & McEvilly, T. v, 1999. Fault Slip Rates at Depth from Recurrence Intervals of Repeating Microearthquakes. *A. A. Koulakov and B. I. Shklovskii Phys. Rev. B*, Vol. 27.
Nakanishi, A., Takahashi, N., Yamamoto, Y., Takahashi, T., Citak, S.O., Nakamura, T., Obana, K., *et al.*, 2018. Three-dimensional plate geometry and P-wave velocity models of the subduction zone in SW Japan: Implications for seismogenesis. *Special Paper of the Geological Society of America*, **534**, 69–86, Geological Society of America. doi:10.1130/2018.2534(04)
Nakata, R., Ando, R., Hori, T. & Ide, S., 2011. Generation mechanism of slow earthquakes: Numerical analysis based on a dynamic model with brittle-ductile mixed fault heterogeneity. *J Geophys Res Solid Earth*, **116**, Blackwell Publishing Ltd. doi:10.1029/2010JB008188
National Research Institute for Earth Science and Disaster Resilience, 2019. NIED F-net.

763 doi:10.17598/NIED.0005
764 Obara, K., 2002. Nonvolcanic Deep Tremor Associated with Subduction in Southwest Japan.
765 *Science (1979)*, **296**, 1679–1681. doi:10.1126/science.1070378
766 Obara, K. & Ito, Y., 2005. Very low frequency earthquakes excited by the 2004 off Kii peninsula
767 earthquakes: A dynamic deformation process in the large accretionary prism. *Earth, Planets*
768 *and Space*, **57**, 321–326. doi:10.1186/BF03352570
769 Obara, K. & Kato, A., 2016. Connecting slow earthquakes to huge earthquakes. *Science*, **353**,
770 253–257. doi:10.1126/science.aaf1512
771 Ohta, K. & Ide, S., 2017. Resolving the Detailed Spatiotemporal Slip Evolution of Deep Tremor
772 in Western Japan. *J Geophys Res Solid Earth*, **122**, 10,009-10,036.
773 doi:10.1002/2017JB014494
774 Ruiz, S., Metois, N., Fuenzalida, A., Ruiz, J., Leyton, F., Grandin, R., Vigny, C., Madariaga, R.,
775 & Campos, J. 2014. Intense foreshocks and a slow slip event preceded the 2014 Iquique Mw
776 8.1 earthquake. Science, 345(6201), 1165-1169. doi:10.1126/science.1256074
777 Shelly, D.R., Beroza, G.C., Ide, S. & Nakamula, S., 2006. Low-frequency earthquakes in Shikoku,
778 Japan, and their relationship to episodic tremor and slip. *Nature*, **442**, 188–191.
779 doi:10.1038/nature04931
780 Takemoto, T., Furumura, T., Saito, T., Maeda, T. & Noguchi, S., 2012. Spatial- and frequency-
781 dependent properties of site amplification factors in Japan derived by the coda normalization
782 method. *Bulletin of the Seismological Society of America*, **102**, 1462–1476.
783 doi:10.1785/0120110188
784 Takemura, S., Baba, S., Yabe, S., Emoto, K., Shiomi, K. & Matsuzawa, T., 2022a. Source
785 Characteristics and Along-Strike Variations of Shallow Very Low Frequency Earthquake
786 Swarms on the Nankai Trough Shallow Plate Boundary. *Geophys Res Lett*, **49**, John Wiley
787 and Sons Inc. doi:10.1029/2022GL097979
788 Takemura, S., Matsuzawa, T., Noda, A., Tonegawa, T., Asano, Y., Kimura, T. & Shiomi, K., 2019.
789 Structural Characteristics of the Nankai Trough Shallow Plate Boundary Inferred From
790 Shallow Very Low Frequency Earthquakes. *Geophys Res Lett*, **46**, 4192–4201.
791 doi:10.1029/2019GL082448
792 Takemura, S., Obara, K., Shiomi, K. & Baba, S., 2022b. Spatiotemporal Variations of Shallow
793 Very Low Frequency Earthquake Activity Southeast Off the Kii Peninsula, Along the
794 Nankai Trough, Japan. *J Geophys Res Solid Earth*, **127**, John Wiley and Sons Inc.
795 doi:10.1029/2021JB023073
796 Takemura, S., Okuwaki, R., Kubota, T., Shiomi, K., Kimura, T. & Noda, A., 2020. Centroid
797 moment tensor inversions of offshore earthquakes using a three-dimensional velocity
798 structure model: slip distributions on the plate boundary along the Nankai Trough. *Geophys*

J Int, **222**, 1109–1125, Oxford University Press. doi:10.1093/gji/ggaa238

Tonegawa, T., Yamashita, Y., Takahashi, T., Shinohara, M., Ishihara, Y., Kodaira, S. & Kaneda, Y., 2020. Spatial relationship between shallow very low frequency earthquakes and the subducted Kyushu-Palau Ridge in the Hyuga-nada region of the Nankai subduction zone. *Geophys J Int*, 1542–1554, Oxford University Press. doi:10.1093/gji/ggaa264

Uchida, N. & Matsuzawa, T., 2011. Coupling coefficient, hierarchical structure, and earthquake cycle for the source area of the 2011 off the Pacific coast of Tohoku earthquake inferred from small repeating earthquake data. *Earth, Planets and Space*, **63**, 675–679, Springer Berlin. doi:10.5047/eps.2011.07.006

Uchida, N., Matsuzawa, T., Hasegawa, A. & Igarashi, T., 2003. Interplate quasi-static slip off Sanriku, NE Japan, estimated from repeating earthquakes. *Geophys Res Lett*, **30**, American Geophysical Union. doi:10.1029/2003GL017452

Voss, N., Dixon, T.H., Liu, Z., Malservisi, R., Protti, M. & Schwartz, S., 2018. Do slow slip events trigger large and great megathrust earthquakes? *Sci Adv*, **4**, 1–6. doi:10.1126/sciadv.aat8472

Wang, K. & Bilek, S.L., 2011. Do subducting seamounts generate or stop large earthquakes? *Geology*, **39**, 819–822, Geological Society of America. doi:10.1130/G31856.1

Wang, Q.-Y., Frank, W.B., Abercrombie, R.E., Obara, K. & Kato, A., 2023. P L A N E TA R Y S C I E N C E What makes low-frequency earthquakes low frequency. Retrieved from https://www.science.org

Wessel, P., Smith, W.H.F., Scharroo, R., Luis, J. & Wobbe, F., 2013. Generic mapping tools: Improved version released. *Eos (Washington DC)*, **94**, 409–410. doi:10.1002/2013EO450001

Yabe, S., Baba, S., Tonegawa, T., Nakano, M. & Takemura, S., 2021. Seismic energy radiation and along-strike heterogeneities of shallow tectonic tremors at the Nankai Trough and Japan Trench. *Tectonophysics*, 228714, Elsevier B.V. doi:10.1016/j.tecto.2020.228714

Yabe, S., Tonegawa, T. & Nakano, M., 2019. Scaled Energy Estimation for Shallow Slow Earthquakes. *J Geophys Res Solid Earth*, **124**, 1507–1519. doi:10.1029/2018JB016815

Yamamoto, Y., Ariyoshi, K., Yada, S., Nakano, M. & Hori, T., 2022. Spatio-temporal distribution of shallow very-low-frequency earthquakes between December 2020 and January 2021 in Kumano-nada, Nankai subduction zone, detected by a permanent seafloor seismic network. *Earth, Planets and Space*, **74**, 14. doi:10.1186/s40623-022-01573-x

Yamamoto, Y., Obana, K., Takahashi, T., Nakanishi, A., Kodaira, S. & Kaneda, Y., 2013. Imaging of the subducted kyushu-palau ridge in the hyuga-nada region, western nankai trough subduction zone. *Tectonophysics*, **589**, 90–102. doi:10.1016/j.tecto.2012.12.028

Yamashita, Y, Asano, Y., Shimizu, H., Uchida, K., Hirano, S., Umakoshi, K., Miyamachi, H., *et al.*, 2015. Migrating tremor off southern Kyushu as evidence for slow slip of a shallow

subduction interface. *Science (1979)*, **348**, 676–679. doi:10.1126/science.aaa4242

Yamashita, Y., Shimizu, H. & Goto, K., 2012. Small repeating earthquake activity, interplate quasi-static slip, and interplate coupling in the Hyuga-nada, southwestern Japan subduction zone. *Geophys Res Lett*, **39**, Blackwell Publishing Ltd. doi:10.1029/2012GL051476

Yamashita, Y., Shinohara, M. & Yamada, T., 2021. Shallow tectonic tremor activities in Hyuga-nada, Nankai subduction zone, based on long-term broadband ocean bottom seismic observations. *Earth, Planets and Space*, **73**, 196. doi:10.1186/s40623-021-01533-x

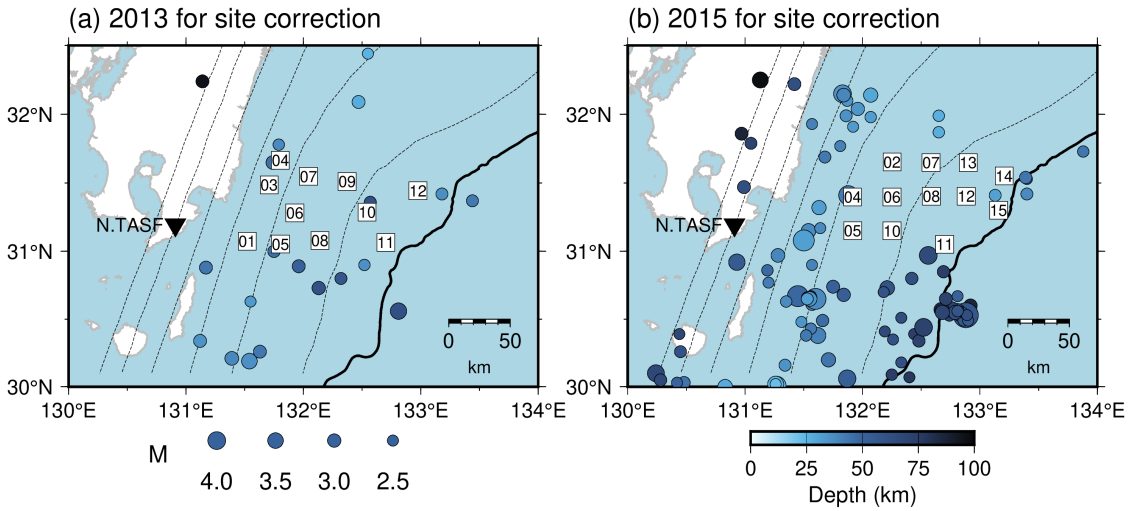

844

845 **Figure S1.** Distribution of earthquakes used for the estimation of the site amplification factors.
846 Inverted triangles display the locations of the F-net stations. Squares represents the locations of
847 OBSs. Black line and dotted contours are the same as displayed in Fig. 6.

848

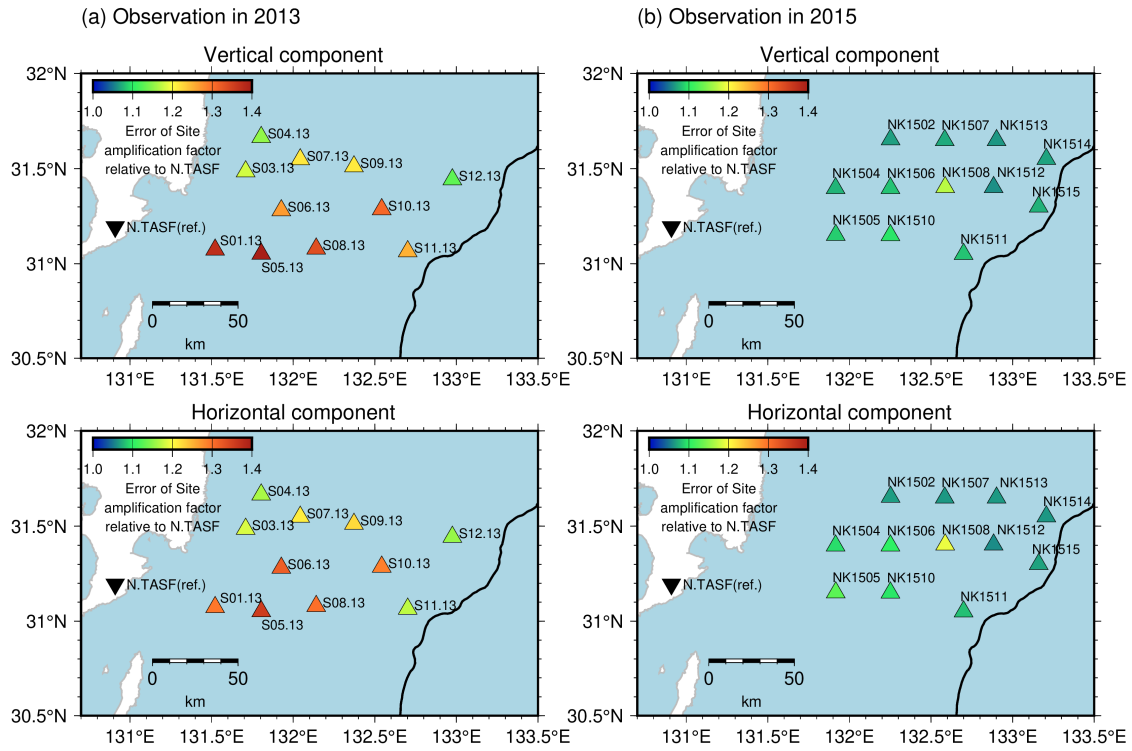

849

850

851 **Figure S2.** Estimation errors of site amplification factors relative to N.TASF at each OBS.
852 Inverted triangle indicates the location of the F-net station, N.TASF. Black line is the same as
853 displayed in Fig. 4.

854

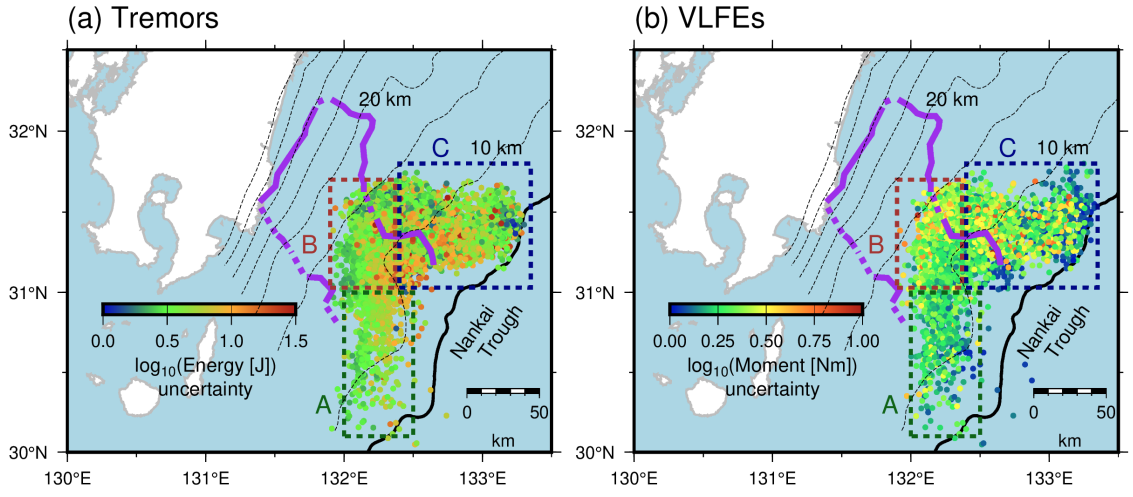

855

856 **Figure S3.** Spatial distribution of the uncertainty of logarithm of (a) tremor energies and (b) VLFE
857 moments. Colored dotted rectangles, dashed contours, purple lines, black line and gray triangles
858 are the same as displayed in Fig. 7.

859

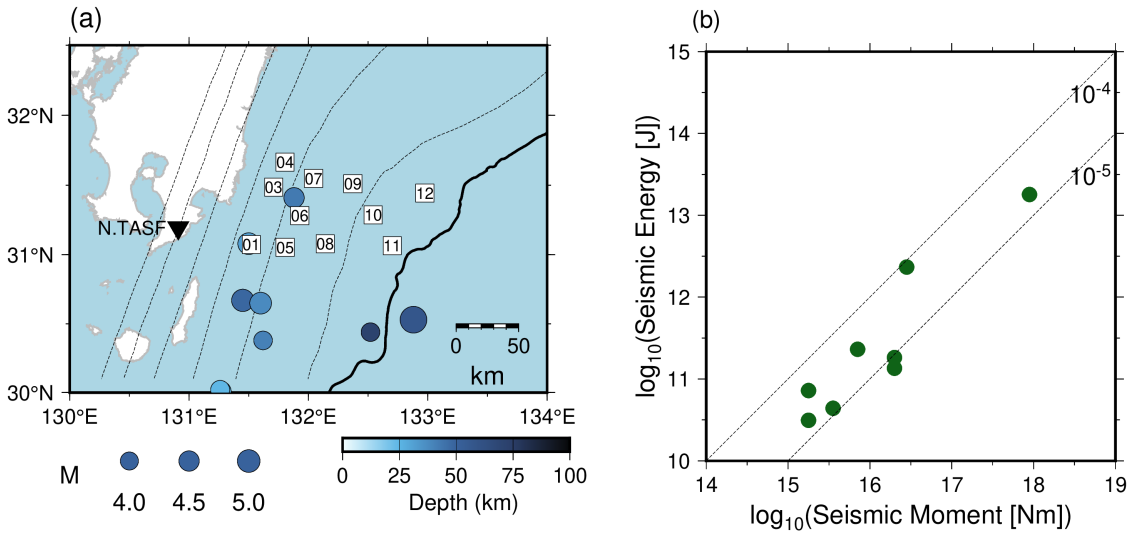

860

861 **Figure S4.** Estimation of seismic energies of regular earthquakes. (a) Distribution of regular
862 earthquakes used for the estimation of seismic energies. Squares are the same as displayed in Fig.
863 S1. Black line and dotted contours are the same as displayed in Fig. 6. (b) Relationship between
864 seismic moment and seismic energy of regular earthquakes shown in Fig. S4a. Seismic moments
865 are calculated from moment magnitude estimated by moment tensor analysis by F-net site
866 (https://www.fnet.bosai.go.jp/event/search.php?LANG=en). Dashed lines represent scaled
867 energies of 10^{-5} and 10^{-4}.

868

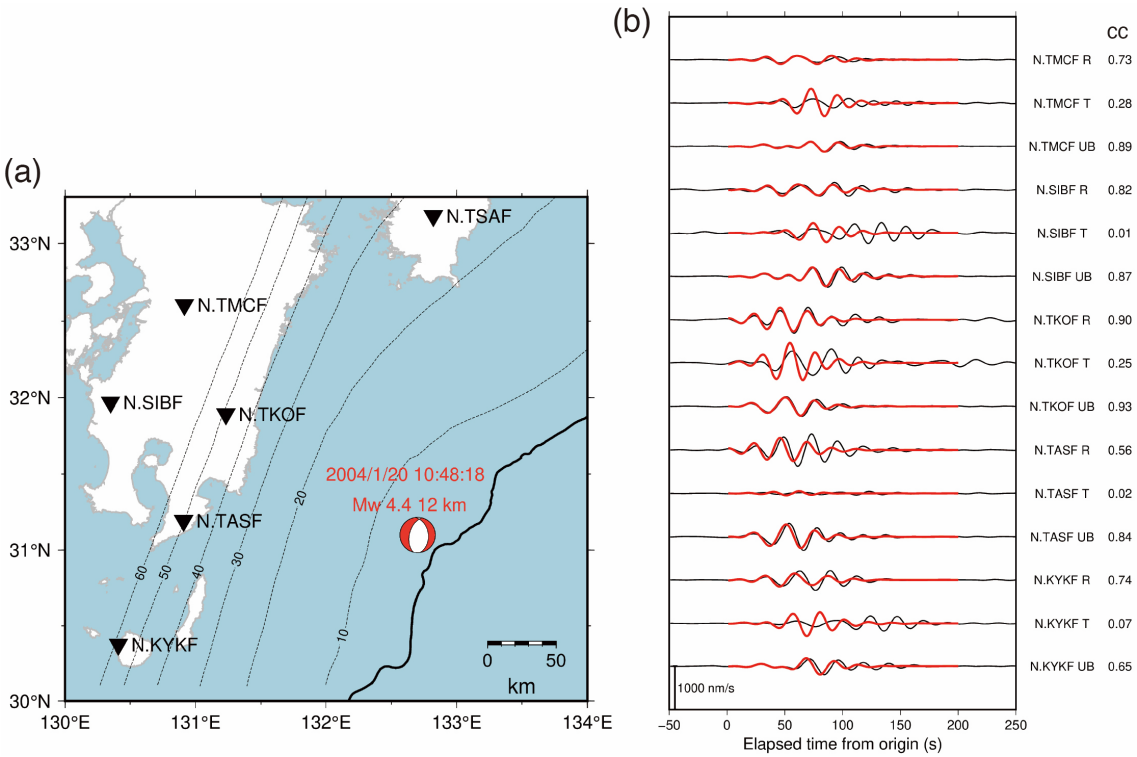

Figure S5. Simulated waveforms of a regular earthquake that occurred in northern Hyuga-nada. (a) Focal mechanism of the regular earthquake listed in the catalog by Takemura et al. (2020; catalog: doi:10.5281/zenodo.3821172). Black line, inverted triangles, and dotted contours are the same as displayed in Fig. 6. (b) Observed (black lines) and simulated (red lines) waveforms of the earthquake at each F-net station. The assumed source time function was a Küpper wavelet with a source duration of 1 s. Black and red lines are the observed and the simulated waveforms, respectively. The simulation setting is the same as described in Section 2.2. R, T, and UB components represent the radial, transverse, and vertical components, respectively.

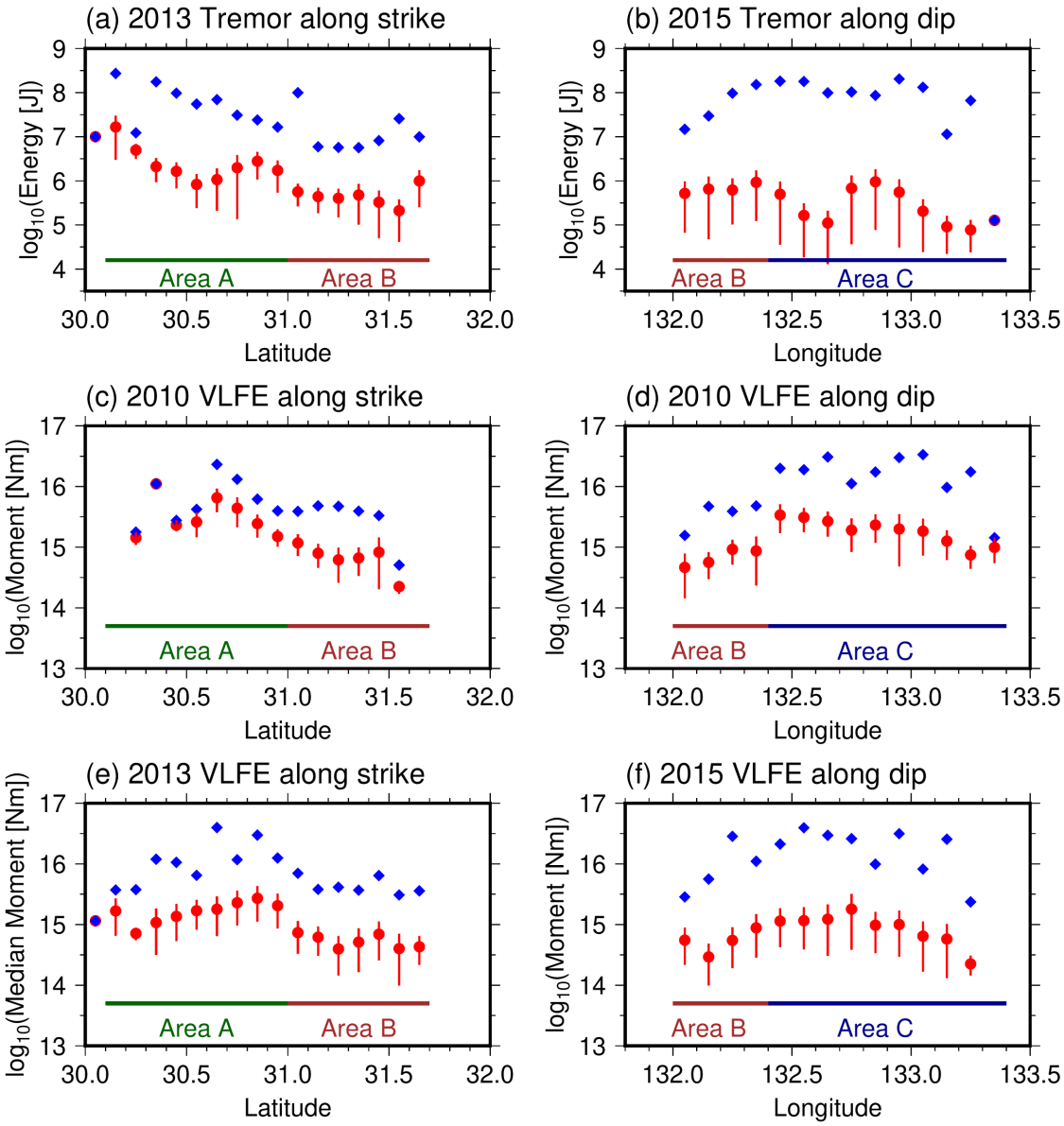

Figure S6. Variation in maximum and median of tremor energies and VLFE moments along strike and dip directions at 0.1° interval. Blue diamonds and red circles represent the maximum and median values, respectively. Red bars show the median absolute deviation of tremor energies and VLFE moments.

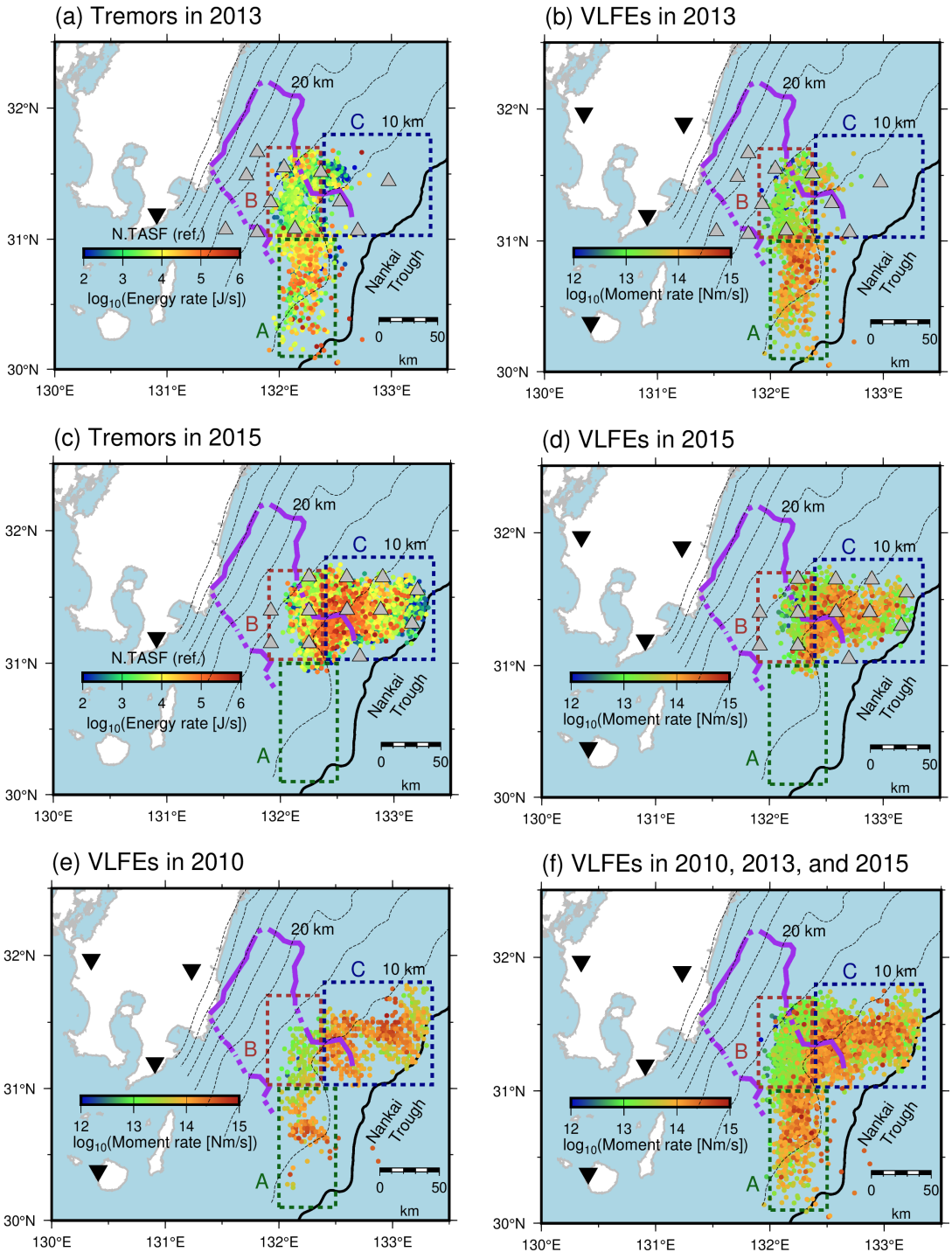

888

889 **Figure S7.** Spatial distribution of (a) energy rates of tremors in 2013, (b) moment rates of VLFEs
890 in 2013, (c) energy rates of tremors in 2015, (d) moment rates of VLFEs in 2015, (e) moment
891 rates of VLFEs in 2010, and (f) moment rates of VLFEs in all analysis periods. Colored dotted
892 rectangles, dashed contours, purple lines, black line and gray triangles are the same as displayed
893 in Fig. 7.

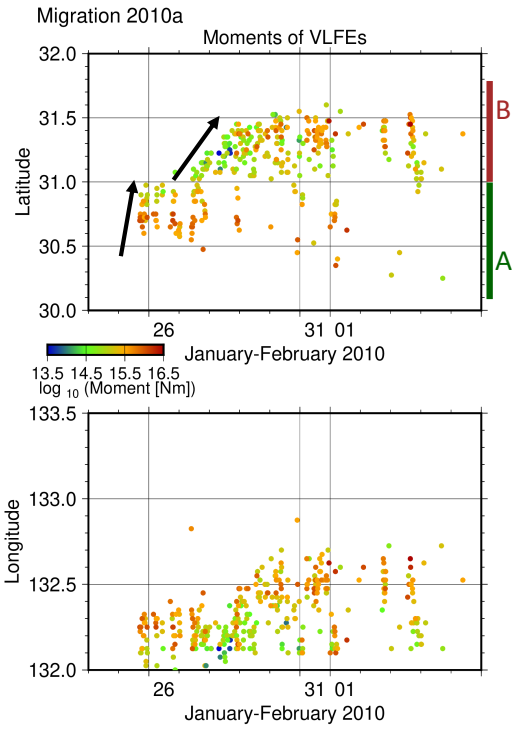

894

895 **Figure S8.** Spatiotemporal distributions of moments of VLFEs in the directions along the N-S
896 and E-W sections for migration of 2010a migration. Black arrows indicate the direction of
897 migrations.

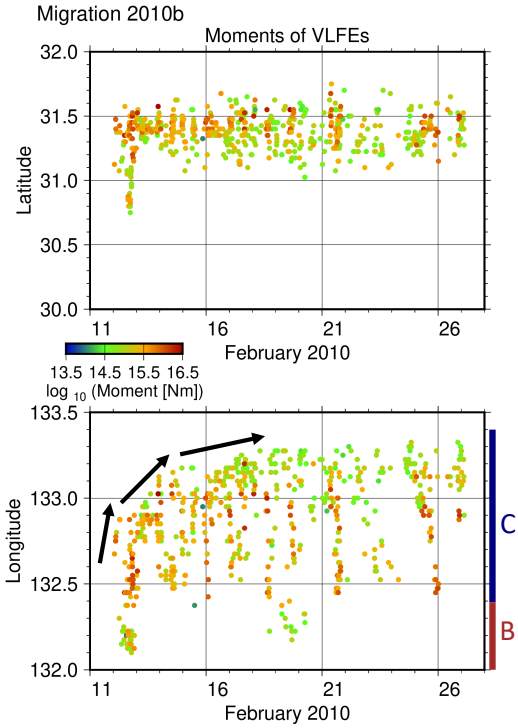

898

899 **Figure S9.** Same as Fig. S8 but 2010b migration.

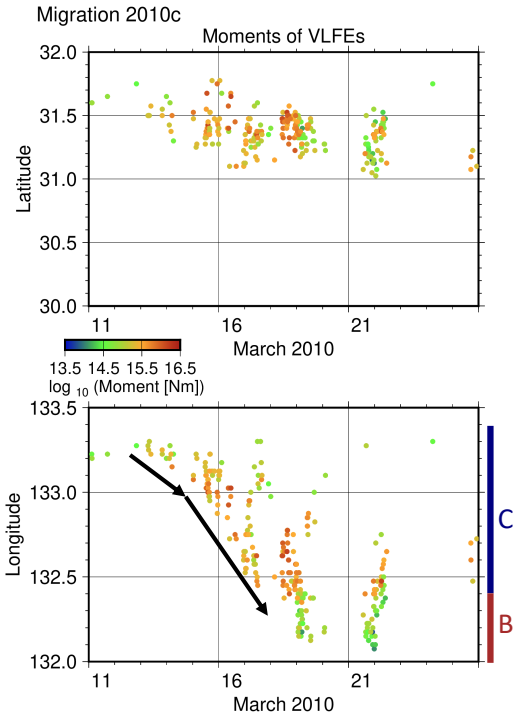

Figure S10. Same as Fig. S8 but 2010c migration.

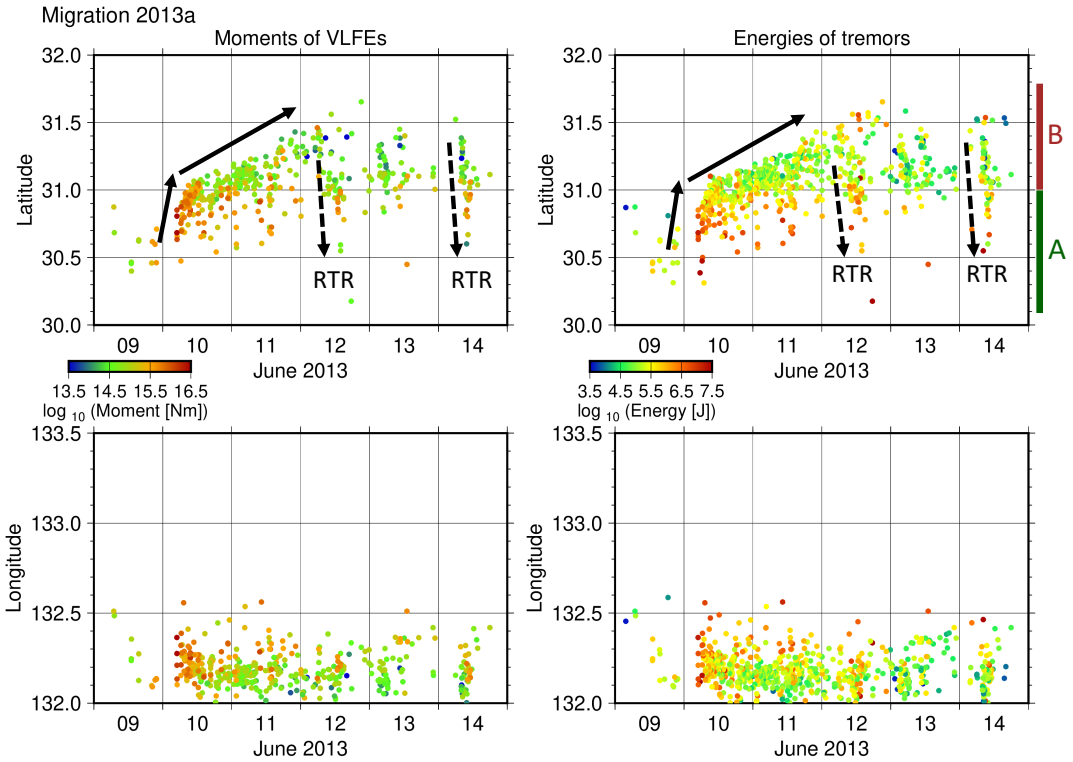

Figure S11. Spatiotemporal distributions of moments of VLFEs and energies of tremors in the directions along the N-S and E-W sections for migration of 2013a migration. Black dotted arrows represent the rapid tremor reversal (RTR).

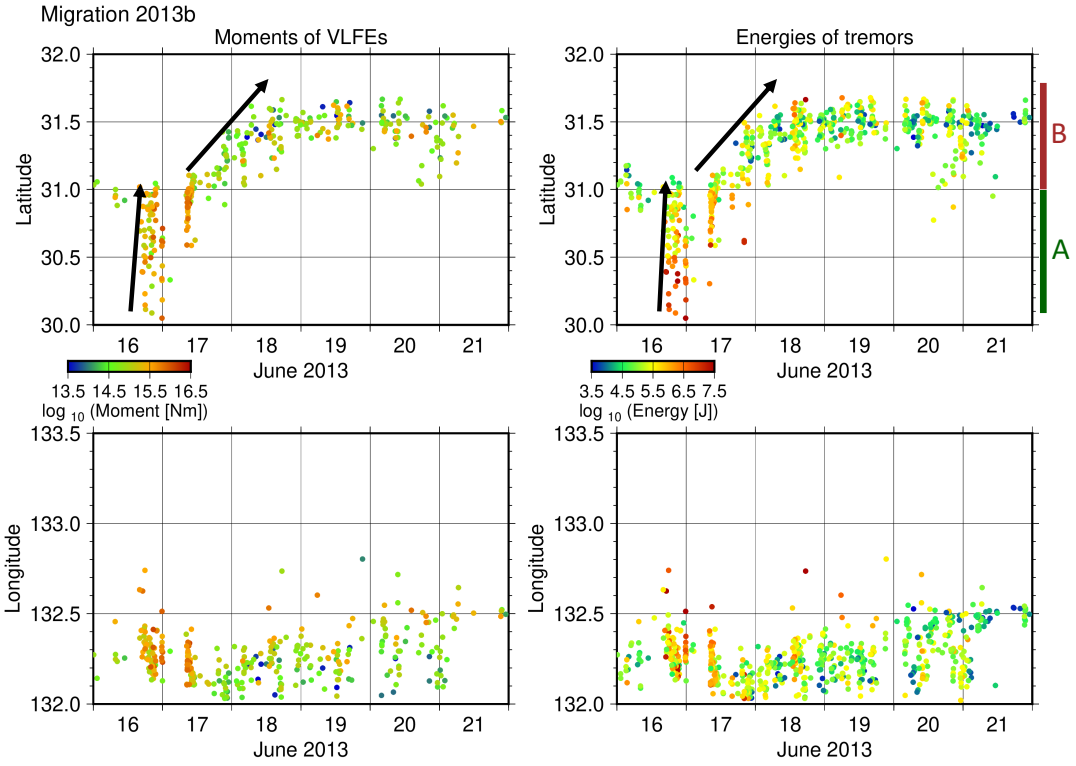

907

908 **Figure S12.** Same as Fig. S11 but 2013b migration.

909

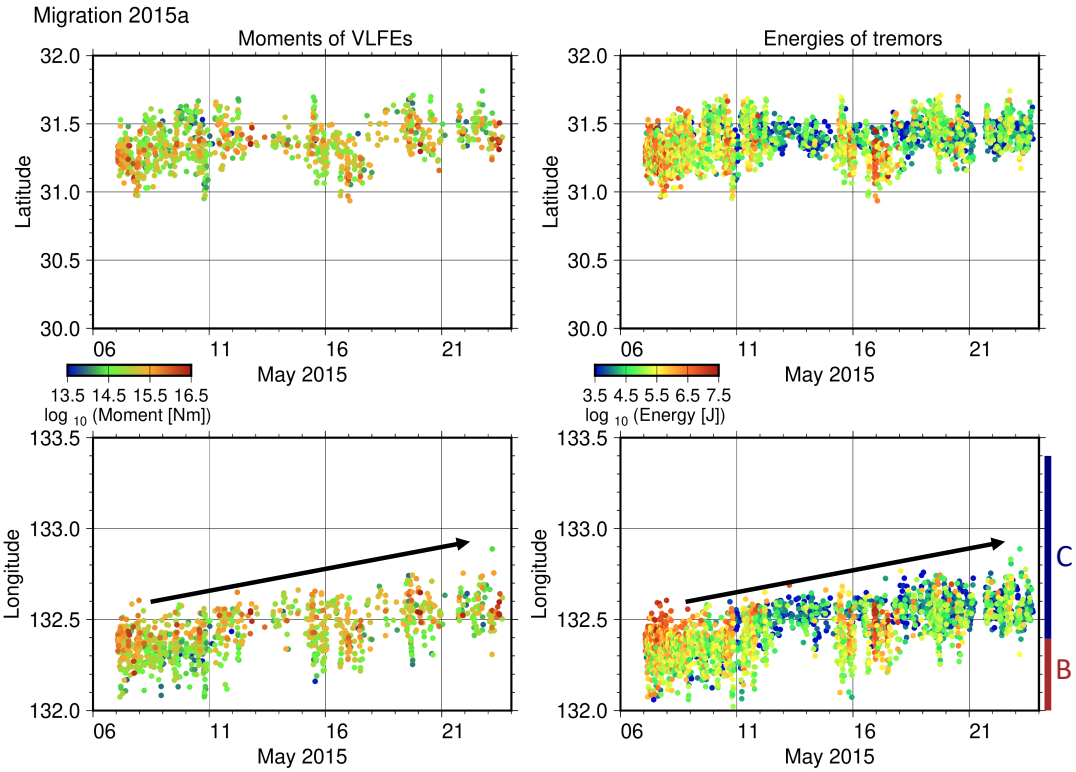

910

911 **Figure S13.** Same as Fig. S11 but 2015a migration.

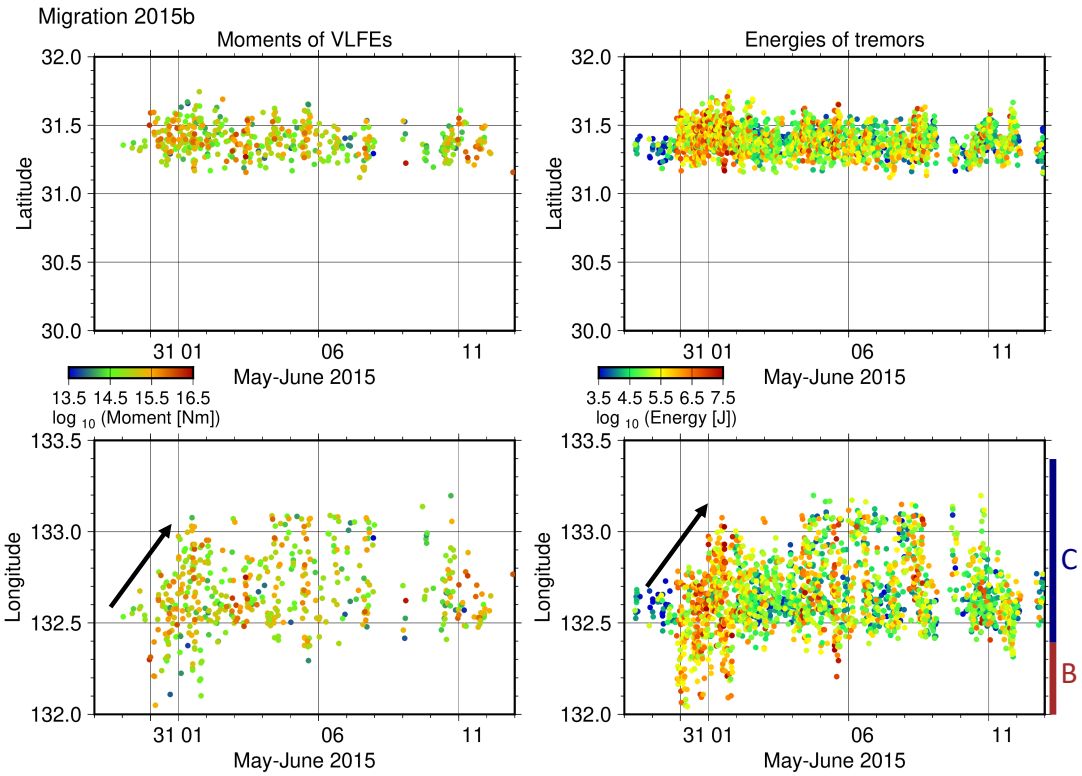

912

913 **Figure S14.** Same as Fig. S11 but 2015b migration.

914

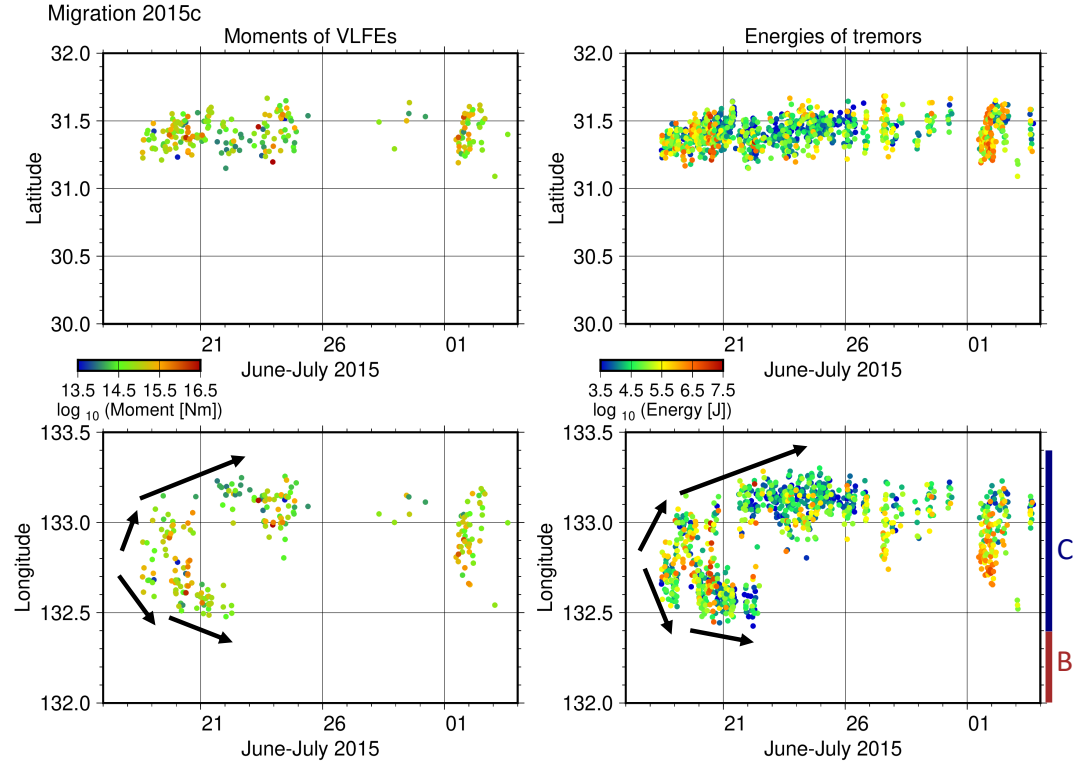

915

916 **Figure S15.** Same as Fig. S11 but 2015c migration.

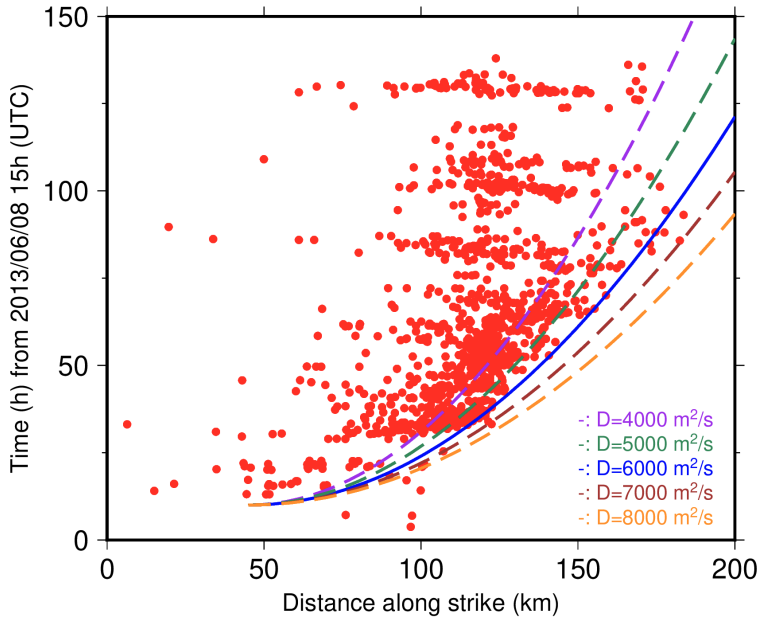

Figure S16. Same as Fig. 11 but with parabolic functions with diffusion coefficients D of 4×10^4 m^2/s, 5×10^4 m^2/s, 6×10^4 m^2/s, 7×10^4 m^2/s, and 8×10^4 m^2/s.

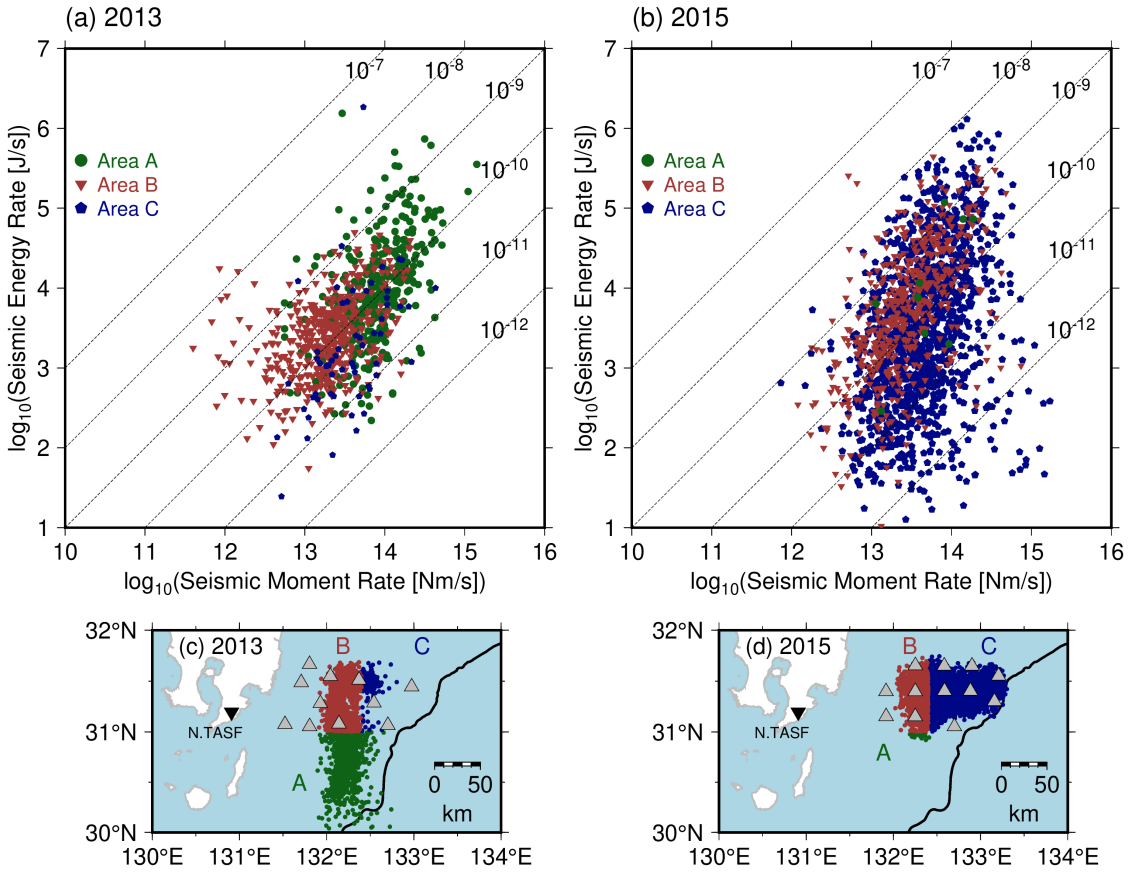

Figure S17. Relationship between seismic moment rates of VLFEs and seismic energy rates of shallow tremors at each area in Hyuga-nada (a) in 2013 and (b) in 2015. Epicentres of shallow tremors at each area (c) in 2013 and (d) in 2015. Shallow tremors in Area A, B, and C are depicted by green, brown, and dark blue dots, respectably. Black lines, gray and black inverted triangles are the same as displayed in Fig.7.

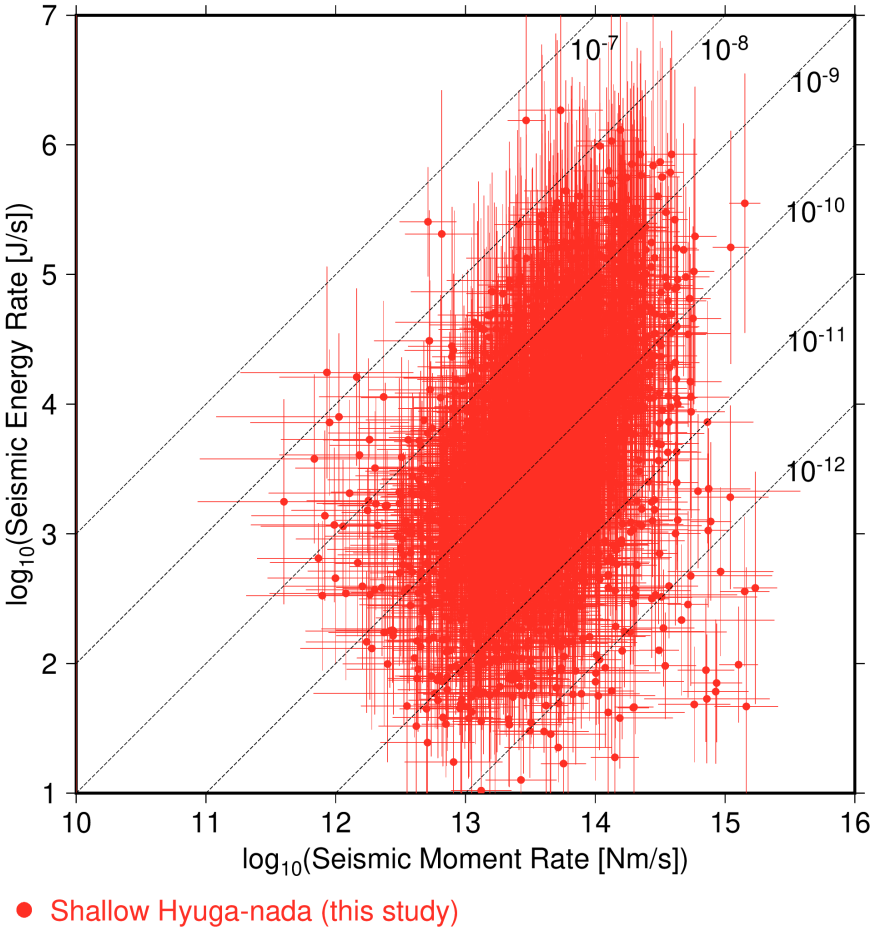

Figure S18. Relationship between seismic moment rates of VLFEs and seismic energy rates of shallow tremors with error bars in Hyuga-nada.

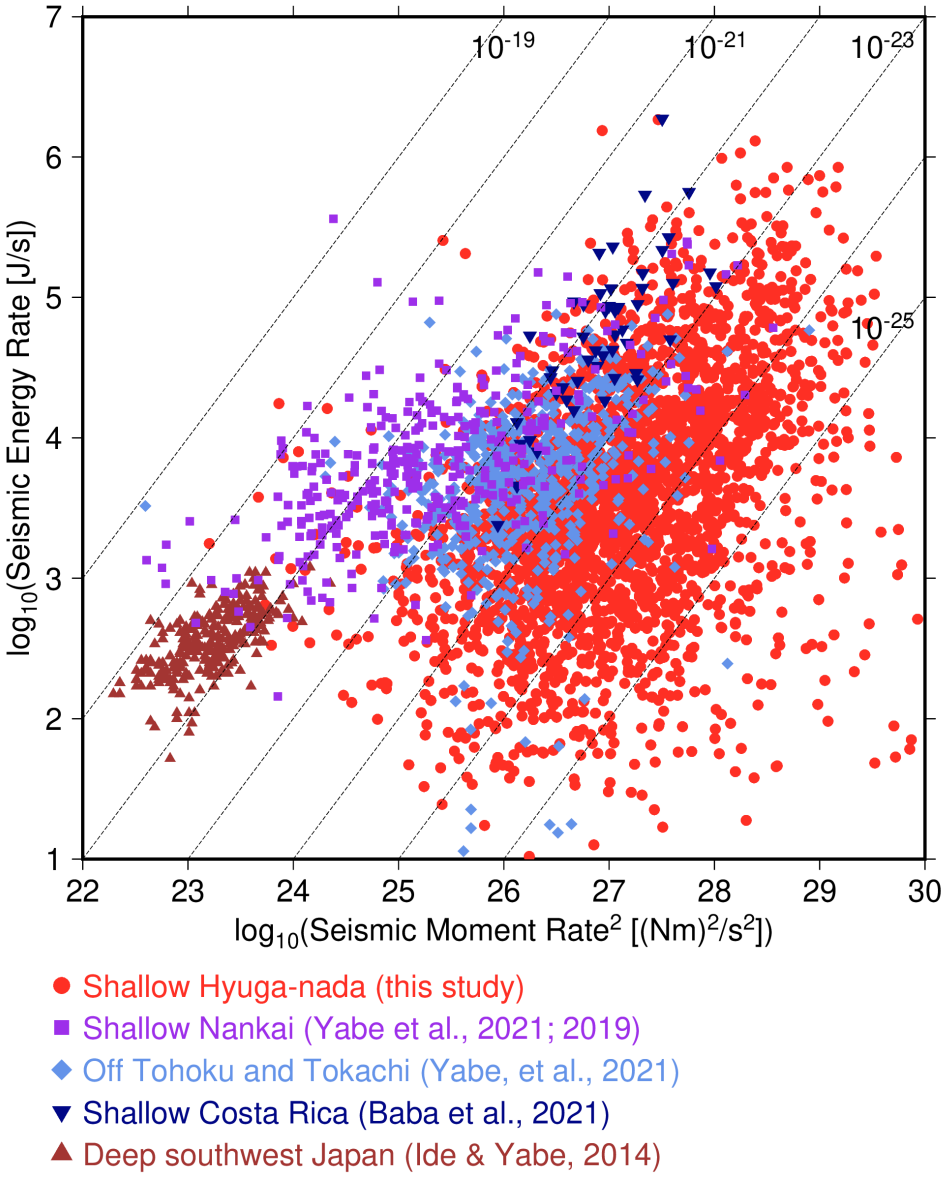

Figure S19. Relationship between seismic moment rates of VLFEs and squared seismic moment rates of tremors. Red circles, purple squares, green diamonds, dark blue inverted triangles, and dark blue triangles indicate the relationships between seismic moment rates of VLFEs and seismic moment rates of tremors in shallow Hyuga-nada (this study), shallow Nankai except Hyuga-nada (Yabe et al. 2021, 2019), off Tohoku and Tokachi (Yabe et al. 2021), shallow Costa Rica (Baba et al. 2021), and deep slow earthquakes (Ide, 2016; Ide and Maury, 2018; Ide and Yabe, 2014).

Table S1. Characteristics of migrations in Hyuga-nada.

	Migration direction	
2010a	Along-strike	South to north
2010b	Along-dip	Downdip to updip
2010c	Along-dip	Updip to downdip
2013a	Along-strike	South to north
2013b	Along-strike	South to north
2015a	Along-dip	Downdip to updip
2015b	Along-dip	Downdip to updip
2015c	Along-dip	Bilateral